

1

2

Effect of tributary inflow on reservoir turbidity current

3

Yining Sun; Ji Li; Zhixian Cao; Alistair G.L. Borthwick; János Józsa

4

5

6 **ABSTRACT**

7 Fluvial flows carrying high sediment loads may plunge into reservoirs to form turbidity
8 currents. However, the effects of tributary inflows on reservoir turbidity currents have
9 remained poorly understood to date. Here a 2D double layer-averaged model is used to
10 investigate a series of laboratory-scale numerical cases. By probing into the
11 hydro-sediment-morphodynamic processes, we find that tributary location and inflow
12 conditions have distinct effects on the formation and propagation of reservoir turbidity
13 currents, and lead to complicated flow dynamics and bed deformation at the confluence. Two
14 flow exchange patterns are generated at the confluence: turbidity current intrusion from the
15 main channel into the tributary; and highly concentrated, sediment-laden flow plunging from
16 the tributary into the turbidity current in the main channel. Tributary sediment-laden inflow
17 causes the stable plunge point to migrate downstream and is conducive to propagation of the
18 turbidity current, whilst the opposite holds in the case of clear-water inflow from the tributary.
19 Heavily sediment-laden inflow from the tributary leads to a considerably higher sediment
20 flushing efficiency by means of the turbidity current. Near the confluence, the planar
21 distributions of velocity and bed shear stress of the turbidity current resemble their
22 counterparts in confluence flows carrying low sediment loads or clear water. Yet, the bed
23 exhibits aggradation near the confluence due to the turbidity current, in contrast to pure scour
24 in a river confluence with a low sediment load. Appropriate account of tributary effects is
25 required in studies of reservoir turbidity currents, and for devising strategies for long-term
26 maintenance of reservoir capacity.

27

28 **KEYWORDS**

29 reservoir; turbidity current; tributary; sediment flushing efficiency; double layer-averaged
30 model

31
32
33
34
35
36
37
38
39
40

Article Highlights

- Tributary inflow may cause the stable plunge point of reservoir turbidity current to migrate either upstream or downstream and modify its propagation.
- Tributary inflow may lead to higher sediment flushing efficiency by reservoir turbidity current.
- Tributary discharge and sediment concentration may lead to disparate bed deformation at confluence.

41 **1 Introduction**

42 Heavily sediment-laden rivers usually involve: flows whose fluid properties have
43 non-Newtonian rheology [1, 2], rapid bed evolution such as bed-tearing scour [3], river
44 blockage [4, 5], active main channel-floodplain interactions leading to disparate
45 morphological patterns in main channels and over floodplains [6], and increased peak
46 discharge along the river [7, 8]. To generate electricity, prevent floods, supply water, and
47 provide irrigation capacity, many large reservoirs have been built on rivers, some of which
48 carry high sediment loads. The hydrological and morphological impacts of large reservoirs
49 can be dramatic, as exemplified by the Yellow River — a river featuring the highest sediment
50 flux in the world [9]. Rivers with high sediment loads, such as the Yellow River and its
51 tributaries in the Loess Plateau, China, often feature extremely complicated
52 flow-sediment-bed interactions. Under certain conditions, subaerial sediment-laden flows in
53 reservoirs may plunge to form turbidity currents as subaqueous sediment-laden flows.
54 Theoretically, turbidity currents exhibit complicated fluid-particle interactions whose
55 mechanisms are not yet fully understood [10, 11]. In practice, turbidity currents are highly
56 desirable for flushing sediment as much as possible out of reservoirs, thereby alleviating
57 sedimentation and capacity loss [12]. Besides advantages in terms of sedimentation, the
58 venting effect of turbidity currents acts as an ecological favour to the downstream
59 environment by transporting fine sediment [13].

60 Over recent decades, many investigations have been undertaken on reservoir turbidity
61 currents [12, 14-17]. Computational modeling has become widely used to resolve the detailed

62 processes of reservoir turbidity currents. Full 3D models (e.g., [18, 19]) are not presently
63 feasible for resolving large-scale turbidity currents, even though they have greater theoretical
64 rigour than 1D and 2D models. As a compromise between computational expense and
65 theoretical accuracy, a coupled 2D layer-averaged model was proposed to resolve turbidity
66 currents in the Xiaolangdi reservoir in the Yellow River [15]. Lai et al. [20] developed a 2D
67 layer-averaged model for turbidity currents that matched results from physical model tests of
68 Shihmen Reservoir, Taiwan. Based on an empirical plunge criterion, Wang et al. [16, 21]
69 proposed a one-dimensional model for open channel flows and turbidity currents while
70 ignoring differences between incipient and stable plunge criteria that have since been
71 revealed by theoretical analysis [22, 23] and flume experiments [24]. Critically, these models
72 can only resolve the propagation of turbidity currents after their formation, and do not reflect
73 the impact of reservoir operation on their formation and propagation. As the present
74 state-of-the-art, the coupled 2D double layer-averaged model proposed by Cao et al. [12] is
75 capable of resolving the whole series of processes behind reservoir turbidity currents, from
76 formation and propagation to recession. This model, along with its recent extended version,
77 has recently been applied to resolve landslide-generated waves, and barrier lake formation
78 and breach processes [25-27].

79 Flow exchange between the main channel (MC) and tributary (TR) can occur either as
80 open channel flow or as a turbidity current in the TR, both of which significantly impact on
81 the evolution of a turbidity current in the MC. Studies have examined the turbidity current in
82 the main river as clear-water flow enters from a TR [16, 21, 28-30]. Intrusion of the turbidity

83 current from the MC to a TR is an essential factor in reducing the discharge and sediment
84 concentration of the current [31], which also advances the location and formation of the
85 plunge point, decelerates the turbidity current, and promotes bed aggradation, causing the
86 sediment flushing efficiency to become relatively small [28]. Several physical experiments
87 have focused on open channel flow in a main river with hyperconcentrated tributary flows
88 [32, 33]. Such conditions lead to increased sediment deposition and more noticeable bars at
89 the confluence than for one experiencing ordinary sediment-laden flow. Nevertheless,
90 previous studies have been mostly limited to turbidity currents arising solely from the MC or
91 a TR. Physically, sediment-laden flows carrying high sediment loads from both the MC and a
92 TR have different characteristics compared to a confluence carrying an ordinary sediment
93 load. In short, the understanding as to how reservoir turbidity currents are modified by
94 tributary inflows is presently far from clear.

95 This paper sets out to unravel the impact of tributary inflow (in terms of discharge,
96 sediment concentration, and junction location) on a reservoir turbidity current in the MC. A
97 coupled 2D double layer-averaged model proposed by Cao et al. [12] is used to investigate a
98 series of laboratory-scale numerical cases. By probing into the computational results, we aim
99 to shed light on the effect of a TR on the formation and propagation of reservoir turbidity
100 currents, and the flow dynamics of turbidity currents near a confluence.

101

102 **2 Methods**

103 A series of laboratory-scale numerical cases are designed on the basis of flume experiments

104 on reservoir turbidity currents by Lee and Yu [24], along with presumed tributary settings and
105 inflows (Fig. 1). A 2D double layer-averaged SHSM model [12] is applied to resolve the flow
106 and sediment transport processes. Based on the numerical results, the impacts of tributary
107 inflow on reservoir turbidity current are evaluated. The methods are briefly described as
108 follows. (See Text S1 in the online Support Information for further details.)

109

110 **2.1 2D hydro-sediment-morphodynamic model**

111 The 2D double layer-averaged model proposed by Cao et al. [12] has been benchmarked
112 against a series of experimental turbidity currents related to lock-exchange [34] and sustained
113 inflows [24], and also successfully applied to the whole process of turbidity currents in the
114 Xiaolangdi Reservoir in the middle Yellow River, China. The model has been further
115 extended to investigate wave and sediment transport processes due to landslides impacting
116 reservoirs [24] as well as barrier lake formation and breach processes [25]. This model is
117 applied in the present study, as outlined below.

118 The governing equations are derived from the fundamental conservation laws in fluid
119 dynamics under the framework of shallow water hydrodynamics, including mass and
120 momentum conservation equations for the upper clear-water flow layer and the lower
121 sediment-laden flow layer (e.g., turbidity current), the mass conservation equation for
122 sediment carried by the turbidity current, and the mass conservation equation for bed
123 sediment. For the upper layer, ρ_w is the density of water, h_w denotes thickness, u_w and
124 v_w are the layer-averaged velocity components in the x - and y -directions. For the lower layer,

125 ρ_s is the density of sediment, $\rho_c = \rho_w(1-c_s) + \rho_s c_s$ is the density of the water-sediment
126 mixture, h_s denotes thickness, u_s and v_s are the layer-averaged velocity components in
127 the x - and y -directions, and c_s is the total volumetric sediment concentration. Bed elevation
128 is denoted by z_b .

129 A set of relationships is introduced to determine the bed resistance and interface shear
130 stress, water entrainment E_w , and net sediment exchange flux (i.e., entrainment E minus
131 deposition D). Specifically, Manning's formula is used to calculate bed shear stresses. Shear
132 stresses at the interface between the upper and lower layers are estimated in a similar fashion.
133 Water entrainment at the interface is calculated using the Richardson number, following
134 Parker et al. [35]. Sediment deposition is determined using the sediment particle settling
135 velocity and near-bed concentration. Bed entrainment flux is estimated using Zhang and Xie's
136 formula for suspended sediment transport capacity [36].

137 The governing equations of the model proposed by Cao et al. [12] are synchronously
138 solved as two hyperbolic systems, one for the upper layer, the other for the lower layer. Each
139 hyperbolic system is solved by a quasi-well-balanced numerical algorithm involving drying
140 and wetting, using an accurate finite volume Godunov-type approach in conjunction with the
141 HLLC (Harten-Lax-van Leer Contact Wave) approximate Riemann solver on a fixed
142 rectangular mesh. The present numerical scheme is explicit, and so the time step is controlled
143 by the Courant-Friedrichs-Lewy condition.

144

145 2.2 Test cases

146 The series of laboratory-scale numerical cases are designed to complement flume
147 experiments by Lee and Yu [24]. As the experiments originally did not involve a tributary
148 (TR), a hypothetical TR is herewith set to the right-hand side of the main channel (MC), with
149 the TR meeting the MC at a junction angle θ of 90° or 45° . Two junction locations are
150 considered, i.e., $L = 5\text{m}, 10\text{m}$. The MC dimensions are $20 \times 0.2 \times 0.6\text{m}$, and its bottom
151 slope is $i_{bm} = 0.02$. The hypothetical TR is rectangular and 17 m long by 0.30 m deep, with
152 0.1 m or 0.2 m width. The TR-to-MC width ratio is defined by $W_r = W_t/W_m$, where W_t and
153 W_m are the widths of TR and MC. The bed slope of the TR can also be adjusted, and two
154 values of bed slope, $i_{bt} = 0.012, 0.02$, are considered (Fig. 1). In the experiments of Lee and
155 Yu [27], there was no bottom outlet for sediment flushing at the downstream end of the flume.
156 Herein a dam is located at the downstream end of the flume, and a bottom sediment flushing
157 tunnel (BSFT) controlled by a bottom sluice gate, 4 cm high, is set for sediment flushing,
158 following Cao et al. [12].

159 Based on combinations of different inflows from the MC and TR, three series of
160 numerical cases are designed as summarized in Table 1, i.e., Series A for sediment-laden flow
161 from the MC without a TR; Series B for sediment-laden flow from the MC with clear-water
162 flow from the TR; Series C for sediment-laden flows from both the MC and TR. The cases
163 enable the effects of TR-to-MC discharge ratio and sediment concentration ratio to be
164 identified. The TR-to-MC discharge ratio is defined by $Q_r = Q_t/Q_m$, where Q_t and Q_m are
165 discharges of TR and MC. The TR-to-MC sediment concentration ratio is defined by

166 $C_r = C_t/C_m$, where C_t and C_m are the volumetric sediment concentrations of TR and MC.

167 The inflow discharge Q_m is $0.001358\text{m}^3/\text{s}$, and the volumetric sediment concentration

168 C_m is 0.05 or 0.00667. More controls upon the effects of tributary inflow on reservoir

169 turbidity current are considered as the junction angle θ , the width ratio W_r and the bed

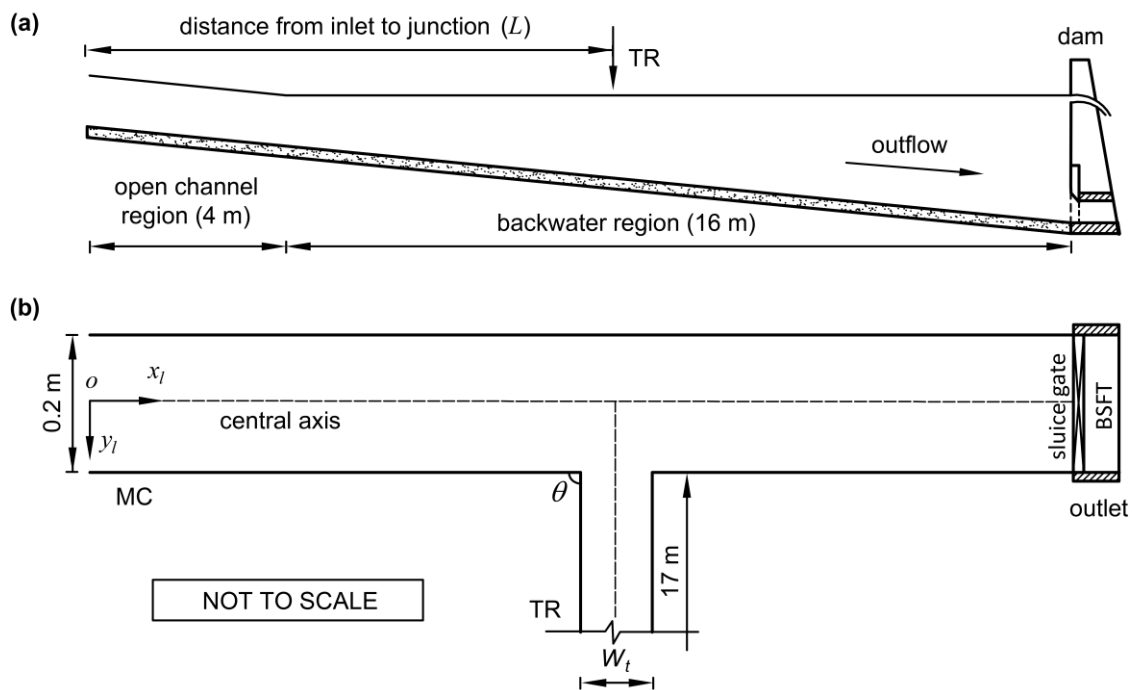
170 slope i_{bt} of the TR. Table 2 summarizes the flow and sediment conditions for Series A-C.

171 The present computations presume initially steady, gradually varied, clear-water flow in

172 accordance with the prescribed discharges in the MC and TR, and an undisturbed water depth

173 of 0.34 m immediately upstream of the dam.

174



175

176 **Fig. 1** Vertical profile (a) and plan view (b) of the main channel (MC) and tributary (TR)

177

178 At the inlet cross-section in the MC, the prescribed discharge and sediment

179 concentration (Table 2) determine the boundary conditions for the subaerial sediment-laden

180 flow layer, when there is no clear-water flow layer. At the inlet cross-section in the TR, if the
 181 inflow contains sediment, the boundary conditions are specified in a similar manner as for the
 182 MC; otherwise, the prescribed discharge (Table 2) is used to specify the boundary condition
 183 for the clear-water flow, when there is no sediment-laden flow layer. The boundary conditions
 184 are implemented using the method of characteristics.

185 At the outlet cross-section, before the arrival of the turbidity current front at the dam, the
 186 bottom sluice gate is closed, and there is no outflow discharge of the turbidity current. The
 187 depth and velocity of the upper clear-water flow layer are determined by the method of
 188 characteristics according to the outflow discharge, Q_{wo} , which is set to be equal to the sum
 189 of inflow discharges from the MC and TR. Upon arrival of the turbidity current front at the
 190 dam, the clear-water outflow of the upper layer is halted, and the bottom sluice gate
 191 simultaneously opened, with the outflow discharge estimated from the following empirical
 192 formula for sluice gate outflow,

$$194 \quad Q_{so} = \mu b e \sqrt{2g'H_0} \quad (1)$$

195
 196 where H_0 is the hydraulic head of the turbidity current, approximated by its elevation H ;
 197 $\mu = 0.60 - 0.176e/H$ is the discharge coefficient; $g' = sg_c$ is the submerged gravitational
 198 acceleration; and $s = (\rho_s/\rho_w) - 1$ is the specific gravity of sediment; the bottom sluice gate
 199 height e is set to 4 cm; and the bottom sluice gate width b is set to 20 cm.

200 The bed roughness Manning coefficient is $n_b = 0.015 \text{ m}^{-1/3} \text{ s}$, and the interface roughness
 201 Manning coefficient is $n_i = 0.005 \text{ m}^{-1/3} \text{ s}$, following Cao et al. [12]. The suspended material is

202 kaolin having a specific gravity of 2.65 and a mean particle size of 6.8 μm . In the
 203 computational model, the converged spatial steps are 0.025 m in both longitudinal and lateral
 204 directions.

205

206 **Table 1.** Arrangement of numerical cases

Series	ID number	Context
A	A1-A2	Sediment-laden flow from MC without TR
B	B1-B12	Sediment-laden flow from MC with clear-water flow from TR
C	C1-C14	Sediment-laden flows from both MC and TR

207

208 **Table 2.** Summary of junction location and inflow conditions for all numerical cases

Series	Junction location		C_m	Ratio			i_{bt}	θ
	$L = 5\text{m}$	$L = 10\text{m}$		Q_r	C_r	W_r		
A	A1		0.05	---	---	---	---	---
	A2		0.00667	---	---	---	---	---
B	B1	B2	0.05	0.736	---	0.5	0.012	90°
	B3	B4	0.05	1.473	---			
	B5	B6	0.00667	0.736	---			
	B7	B8	0.05	1.473	---	1.0	0.02	45°
	B9	B10	0.05	1.473	---	0.5		
	B11	B12	0.05	1.473	---	---	0.012	45°
	C	C1	C2	0.05	0.736	1.334	0.5	0.012
C3		C4	0.05	1.473	0.667			
C5		C6	0.05	1.473	1.334			

C7	C8	0.00667	0.736	0.667			
C9	C10	0.05	1.473	1.334	1.0		
C11	C12	0.05	1.473	1.334		0.02	
C13	C14	0.05	1.473	1.334	0.5	0.012	45°

209

210 **3 Results and discussion**

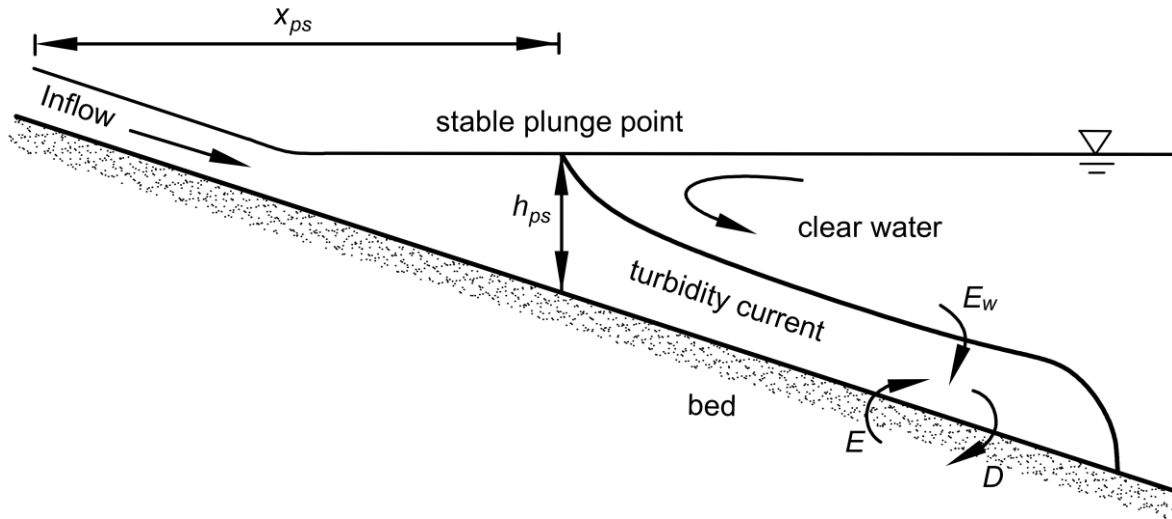
211 **3.1 Characteristics at the plunge point**

212 Here we evaluate the effects of tributary inflow and sediment inputs on the formation of MC
213 turbidity currents based on the numerical results (Cases A1, B1-B4, C1-C6 in Table 2). The
214 transition from subaerial open channel sediment-laden flow to subaqueous turbid flow
215 features reservoir turbidity current formation, with unstable plunge points that initially move
216 forward. By $t \sim 100$ s, the plunge points have stabilized in Cases A1, B1-B4 and C1-C6, and
217 the turbidity current fronts have not yet arrived at the bottom outlet.

218 Fig. 2 shows a definition sketch of the stable plunge region along the central axis of MC,
219 where x_{ps} is the distance between the stable plunge point and main flume entrance; h_{ps} is
220 the turbidity current thickness at the stable plunge point; E_w is the mass flux of water
221 entrainment across the interface between the two layers; and E, D are the sediment
222 entrainment and deposition fluxes. Table 3 lists the location x_{ps} , depth h_{ps} , and densimetric
223 Froude number $F_{ps} = u_s / \sqrt{sgc_s h_{ps}}$ at stable plunge points along the central axis of the MC,
224 corresponding to the different inflow conditions and junction locations considered (Cases A1,
225 B1-B4, C1-C6 in Table 2). Fig. 3a displays the locations of stable plunge points in the MC.
226 Later, in all cases by $t > 120$ s, the turbidity currents become able to flush sediment through

227 the BSFT, and the plunge point gradually changes location, as indicated in Fig. 3b at $t = 2$ h.

228



229

230 **Fig. 2** Definition sketch of reservoir flow featuring turbidity current

231

232 **Table 3** Parameters of stable plunge points along central axis of MC at $t = 100$ s

Q_r	C_r	$L = 5\text{m}$			$L = 10\text{m}$				
		Case	x_{ps} (m)	h_{ps} (cm)	F_{ps}	Case	x_{ps} (m)	h_{ps} (cm)	F_{ps}
—	—	A1	5.375	4.74	0.67	—	—	—	—
0.736	—	B1	4.95	4.80	0.67	B2	5.35	4.78	0.66
	1.334	C1	6.20	6.07	0.75	C2	5.55	4.81	0.65
1.473	—	B3	4.875	4.65	0.68	B4	5.275	4.77	0.66
	0.667	C3	7.60	8.86	0.77	C4	5.575	4.87	0.67
	1.334	C5	6.80	7.45	0.76	C6	5.55	4.86	0.66

233

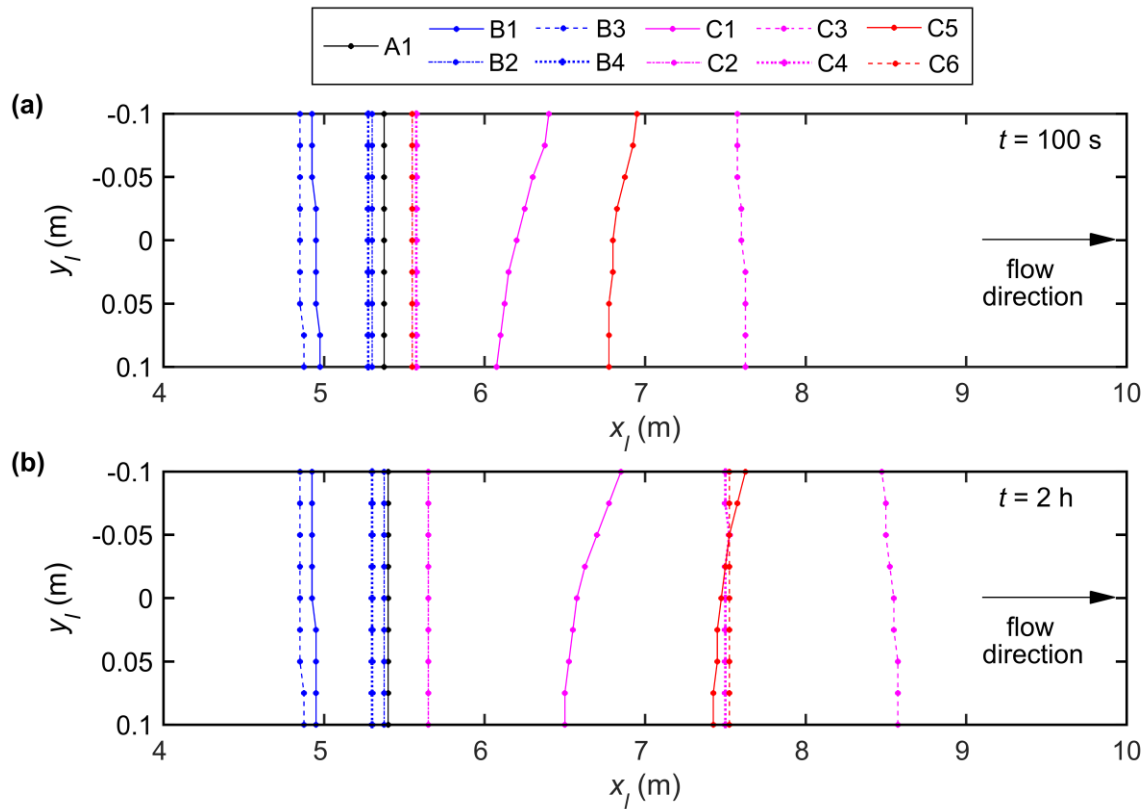
234 Table 3 and Fig. 3a present flow parameters at the stable plunge point at $t = 100$ s for

235 Cases A1, B1-B4 and C1-C6. For convenience, we define the stable plunge point of reservoir

236 turbidity current in the case without a TR as the original stable plunge point (OSPP). For
237 Cases A1, B1-B4 and C1-C6, OSPP locates at $x_j = 5.375\text{m}$. Clear-water flow from the TR
238 causes the stable plunge point to migrate upstream of the OSPP, as demonstrated in Cases
239 B1-B4. However, heavily sediment-laden inflow from the TR increases the discharge and
240 sediment concentration of the MC turbidity current, causing its stable plunge point to migrate
241 downstream of the OSPP. After 2 hrs, the plunge point in Series C cases migrates further
242 downstream, characterizing the feedback effect of significant bed deformation (subsection
243 3.6), whereas the plunge point position in the other Series A and Series B cases hardly
244 changes with time (Fig. 3b).

245 Tributary inflow conditions and junction location lead to distinct effects on the plunge
246 point of the turbidity current in the MC. We consider two junction locations, $L = 5\text{ m}$ and 10
247 m , one of which is located upstream and the other downstream of the OSPP. In Series B, the
248 stable plunge point is located further upstream for the larger discharge ratio, and this effect is
249 most pronounced when the junction is located upstream of the OSPP (Case B3). In Series C,
250 if the junction is located upstream of the OSPP, then x_{ps} , h_{ps} , and F_{ps} along the central
251 axis tend to increase as the tributary inflow discharge increases, but decrease as the tributary
252 sediment concentration increases (Table 3). This occurs primarily because either larger
253 discharge or smaller sediment concentration of the lower sediment-laden flow layer (e.g.,
254 turbidity current) promotes further water entrainment. Furthermore, for $C_r > 1$, the stable
255 plunge point in the MC moves downstream (Cases C1 and C5). For $C_r < 1$, the stable plunge
256 point near the TR migrates downstream (Case C3). For a finite value of sediment

257 concentration ratio, there is a lateral variation in plunge point position. By contrast, if the
 258 junction is located downstream of the OSPP, the effect of tributary inflow on turbidity current
 259 formation is minor (Cases C2, C4 and C6).
 260



261
 262 **Fig. 3** Turbidity current plunge point locations in the MC at (a) $t = 100$ s, (b) $t = 2$ h for
 263 Cases A1, B1-B4, and C1-C6 listed in Tables 2 and 3

264

265 3.2 Advance of turbidity current front

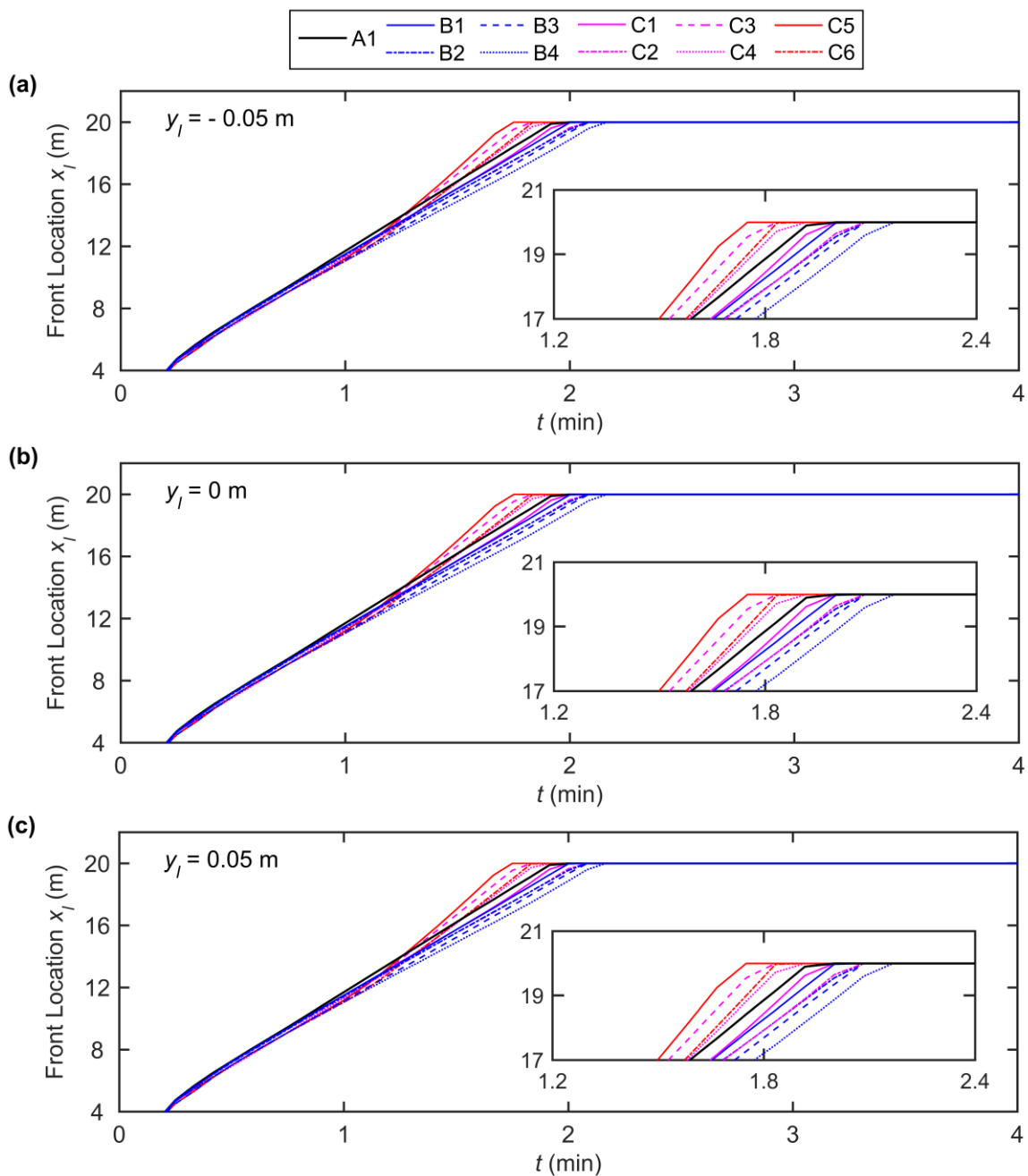
266 Fig. 4 illustrates the front locations of the MC turbidity currents for Cases A1, B1-B4, C1-C6
 267 in Table 2. Hardly any difference is discernible in the front location moving along three lines
 268 across the MC at $y_l = -0.05$ m, 0 m, and 0.05 m, indicating that the tributary inflow
 269 conditions have little effect on the advance of turbidity currents in the lateral direction. In the

270 longitudinal direction, clear-water flow from the TR slows down the propagation of turbidity
271 current, as in the Series B cases. It should be emphasized that the boundary inflows of the
272 MC and TR in Series C are sediment-laden compared to the initial clear-water flows.
273 Therefore, before interacting with the upstream sediment-laden flow entering from the TR,
274 the turbidity current of Series C propagates more slowly than that of Series A. By contrast,
275 the turbidity current of Series C advances faster at a larger discharge ratio as the heavily
276 sediment-laden flow from the TR plunges into the MC turbidity current (Cases C3-C6).

277 Compared to Case A1 without a TR, the MC turbidity current propagation is slower for a
278 larger discharge ratio in Series B (Cases B1 and B3, B2 and B4). Physically, clear-water flow
279 from the TR dilutes the MC turbidity current, while the MC turbidity current simultaneously
280 intrudes into the TR. Both phenomena cause the sediment concentration of the MC turbidity
281 current to reduce, thus reducing the gravity difference between the MC turbidity current and
282 ambient fluid (clear water). Consequently, the MC turbidity current propagates more slowly
283 than in a corresponding case without a TR. By contrast, the larger the discharge of
284 sediment-laden flow from the TR, the faster the turbidity current propagates (Cases C1 and
285 C5, C2 and C6). Furthermore, the higher the sediment concentration (corresponding to a
286 larger driving force) of sediment-laden flow from the TR, the faster the MC turbidity current
287 propagates, as evidenced by Cases C3 and C5, C4 and C6. Tributary effects on the
288 propagation of turbidity current are most evident when the junction is located upstream of the
289 OSPP (Cases C3 and C5).

290 The results are further extended for other values of x_{st} (distance from the junction
291 location to OSPP), corresponding to Fig. S1 shown in the Supporting Information online. Fig.

292 S1 displays the time history of turbidity current front location at the centreline ($y_l = 0\text{ m}$) of
 293 the MC for Cases A2, B5-B6, and C7-C8. It should be noted that the stable plunge point of
 294 Case A2 with smaller volumetric sediment concentration locates further downstream than that
 295 of Case A1. Succinctly, tributary inflow conditions have a discernible effect on front location,
 296 and so warrant appropriate treatment in reservoir sediment management schemes.
 297



298

299 **Fig. 4** Time history of turbidity current front at three transverse locations across the MC: **(a)**
300 $y_l = -0.05$ m ; **(b)** $y_l = 0$ m ; **(c)** $y_l = 0.05$ m for Cases A1, B1-B4, and C1-C6 listed in
301 Tables 2 and 3
302

303 **3.3 Turbidity current thickness**

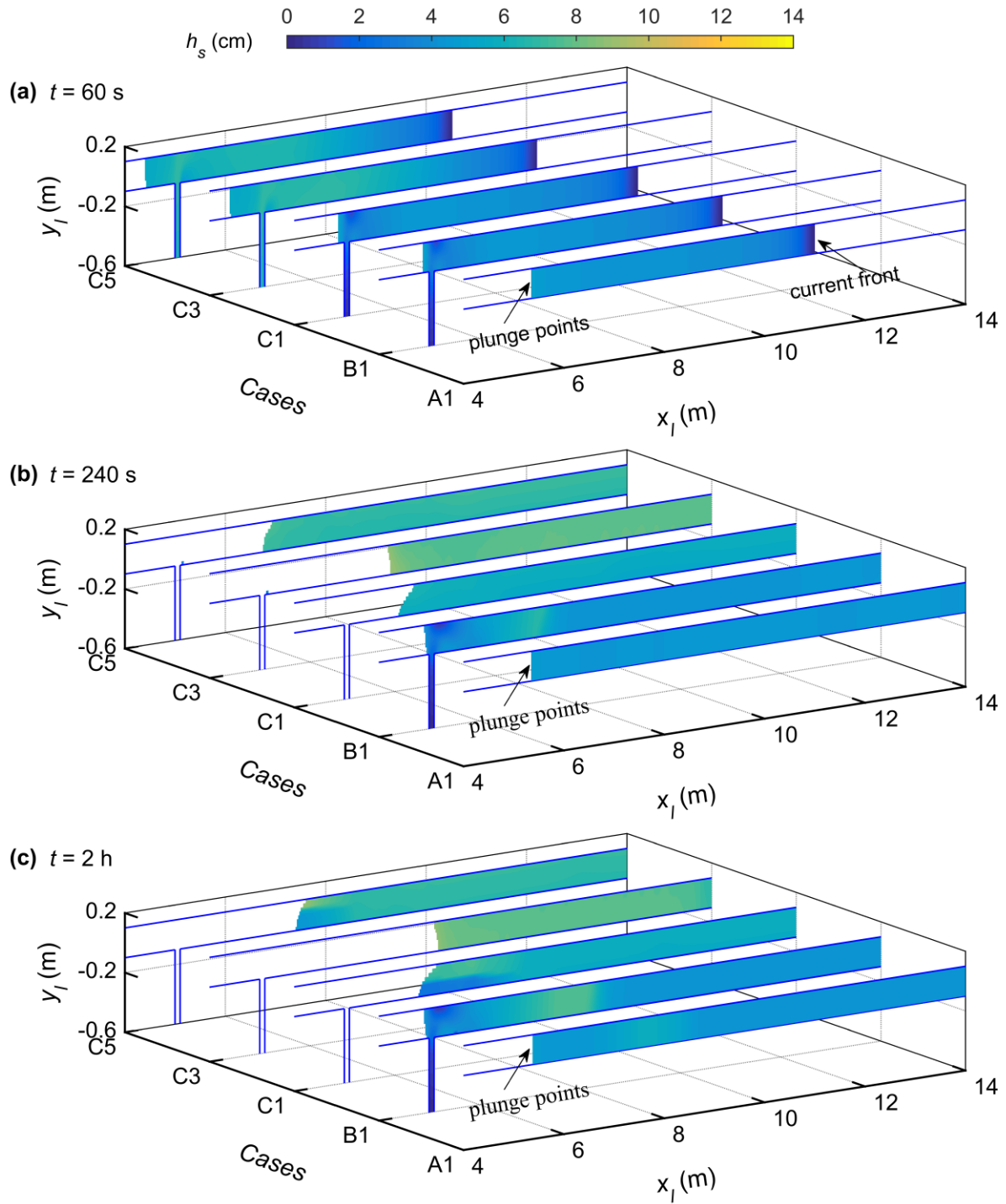
304 We now delve into the effect of tributary inflow on turbidity current thickness. Fig. 5 displays
305 planar distributions of turbidity current thickness for Case A1 without a TR at three time
306 instants ($t = 60$ s, 240s, 2h) and for Cases B1, C1, C3, and C5 when the junction is located
307 upstream of the OSPP. Fig. 6 shows the planar distributions of turbidity current thickness for
308 Cases B2, C2, C4, and C6 when the junction is located downstream of the OSPP.

309 By $t = 60$ s, the subaerial sediment-laden flow in the MC for the Series B and C cases
310 has turned into a turbidity current and intruded from the MC to TR, and so its thickness at the
311 junction is smaller than for Case A1 without a TR (Figs. 5a and 6a). By $t = 240$ s, the
312 turbidity current fronts in all cases have reached the dam (Fig. 4). In Series C, sediment-laden
313 flow from the TR encounters the MC turbidity current, whose thickness increases at the
314 junction owing to the discharge of water and sediment from the TR (Figs. 5b and 6b).
315 Moreover, in series C, a larger turbidity current thickness is generally obtained with a larger
316 discharge ratio and a lower sediment concentration ratio, as evident in Cases C3 and C5. In
317 Cases B1 and B2 at $t = 2$ h , the MC turbidity current continuously intrudes into the TR, and
318 its thickness at the junction is smaller than Case A1 without a TR. By contrast, for the Series
319 C cases, when the junction is located upstream of the OSPP, the turbidity current thickness in

320 Cases C1 and C5 with $C_r > 1$ is smaller downstream of the junction corner, whereas the
321 turbidity current thickness in Case C3 with $C_r < 1$ is larger without significant lateral
322 variation (Fig. 5c), reflecting the effect of bed deformation near the confluence (subsection
323 3.6). When the junction is located downstream of the OSPP, the thickness at the junction for
324 Cases C2, C4 and C6 is larger than for Case A1 (Fig. 6c).

325 The thickness of a turbidity current at a confluence exhibits high temporal and spatial
326 variability. Differences in flow exchange patterns cause lateral variation in turbidity current
327 thickness at the confluence. Reservoir turbidity current intrusion from the MC to TR leads to
328 smaller turbidity current thickness at the junction than for Case A1 without a TR. However,
329 highly concentrated sediment-laden flow plunging from the TR into the MC turbidity current
330 leads to it having larger longitudinal thickness. This occurs primarily because sediment-laden
331 flow from the TR induces more water and sediment into the MC turbidity current.
332 Nevertheless, in a long-term hydro-sediment-morphodynamic process, the turbidity current
333 thickness is affected by bed deformation and boundary conditions in the reservoir.

334



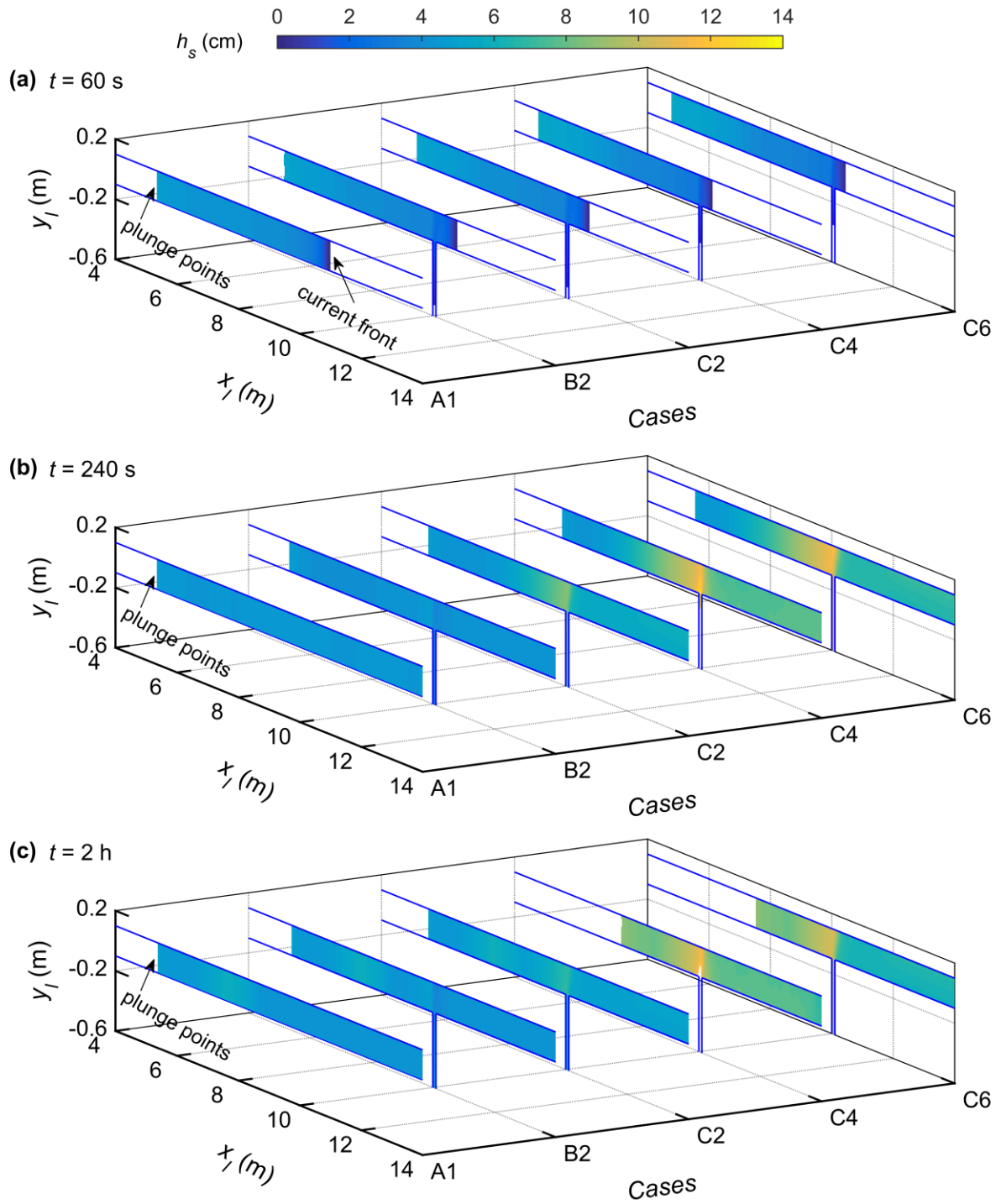
335

336 **Fig. 5** Planar distributions of turbidity current thickness h_s for Cases A1, B1, C1, C3 and C5

337 with the junction is located upstream of the OSPP at (a) $t = 60$ s, (b) $t = 240$ s, and (c)

338 $t = 2$ h

339



340

341 **Fig. 6** Planar distributions of turbidity current thickness h_s for Cases A1, B2, C2, C4 and C6

342 with the junction is located downstream of the OSPP at (a) $t = 60$ s, (b) $t = 240$ s, and (c)

343 $t = 2$ h

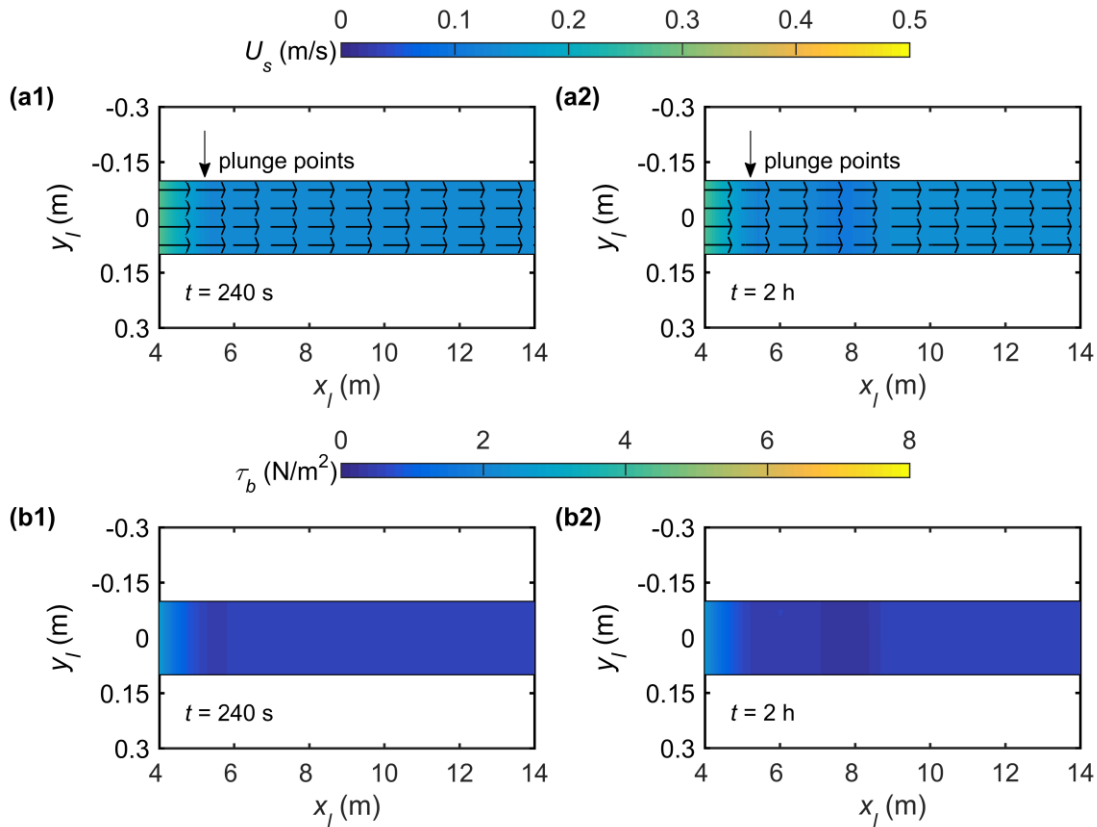
344

345 **3.4 Turbidity current velocity field**

346 We now consider the effect of tributary inflow on the turbidity current velocity field near the
347 confluence. For a reservoir turbidity current with distinct tributary inflow, two flow exchange
348 patterns are generated at the confluence: the reservoir turbidity current intrudes from the MC
349 to TR (Series B), while highly concentrated, sediment-laden flow plunges from the TR into
350 the MC reservoir turbidity current (Series C). Although many research investigations have
351 examined open channel flow at a confluence [37-45], none has considered highly
352 concentrated, sediment-laden flow. A previous experimental study on open channel
353 confluences carrying low sediment loads revealed that the flow structure can be divided into
354 six regions [40]: (i) a stagnation zone with reduced flow velocity at the upstream junction
355 corner between the MC and TR; (ii) a deflection zone at the entry to the junction; (iii) a flow
356 separation zone commencing at the downstream junction corner; (iv) a region of maximum
357 velocity near the centre of the MC just downstream of the junction; (v) a flow recovery area
358 further downstream of the junction; and (vi) shear layers between the two confluence flows.

359 To gain more insight into the flow dynamics of reservoir turbidity currents, we now
360 examine the resultant layer-averaged velocity ($U_s = \sqrt{u_s^2 + v_s^2}$) of the sediment-laden flow
361 layer and associated bed shear stress ($\tau_b = \rho_c g n_b^2 U_s^2 / h_s^{1/3}$) for Cases A1, B3, C5 and C6 at
362 flow elapsed times $t = 240$ s and $t = 2$ h. Fig. 7 depicts the lower layer-averaged velocity field
363 and bed shear stress distribution obtained for Case A1 in the absence of a TR. By $t = 240$ s,
364 subaerial sediment-laden flow in the MC has plunged into the clear water at $x_l = 5.375$ m,
365 whilst the layer-averaged velocity of sediment-laden flow and bed shear stress have

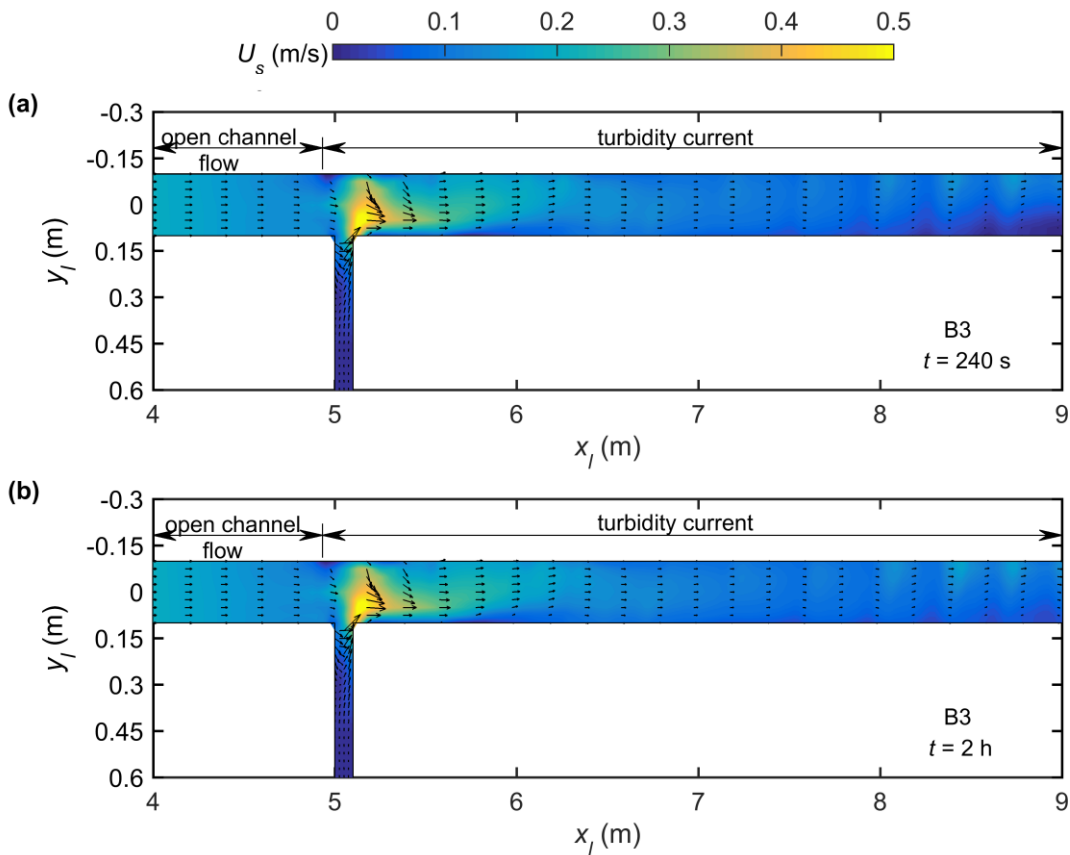
366 decreased owing to propagation of the turbidity current (Figs. 7a1 and 7b1). At $t = 2 \text{ h}$, the
 367 turbidity current velocity field has hardly altered (Fig. 7a2), with the magnitude of bed shear
 368 stress generally below 1.0 N/m^2 (Fig. 7b2).
 369



370
 371 **Fig. 7 (a1-a2)** Velocity field of sediment-laden flow layer and **(b1-b2)** distribution of
 372 magnitude of bed shear stress τ_b for Case A1, at times $t = 240 \text{ s}$ and $t = 2 \text{ h}$

373
 374 Fig. 8 shows the results for Case B3 which features highly concentrated, sediment-laden
 375 flow entering the junction from the MC and clear-water flow from the TR, when the junction
 376 is located upstream of the OSPP. By $t \sim 240 \text{ s}$, the MC turbidity current has reached the
 377 junction and intruded into the TR. The magnitude of the resultant layer-averaged velocity of

378 the turbidity current decreases as it propagates upstream into the TR, and increases at the
 379 downstream junction corner owing to the presence of a small recirculation zone (Fig. 8a).
 380 Again at $t = 2$ h, the velocity field at the confluence hardly changes compared to that at
 381 $t = 240$ s (Fig. 8b). The bed shear stress features are similar to that of the velocity field at the
 382 junction, with the downstream junction corner experiencing a high level of bed shear stress
 383 (Figs. 11a1 and 11a2). There are noticeable differences in the lower-layer averaged velocity
 384 fields and bed shear stress distributions obtained for Series B and Series A cases due to
 385 intrusion of the turbidity current from the MC to the TR (Figs. 7 and 8).
 386

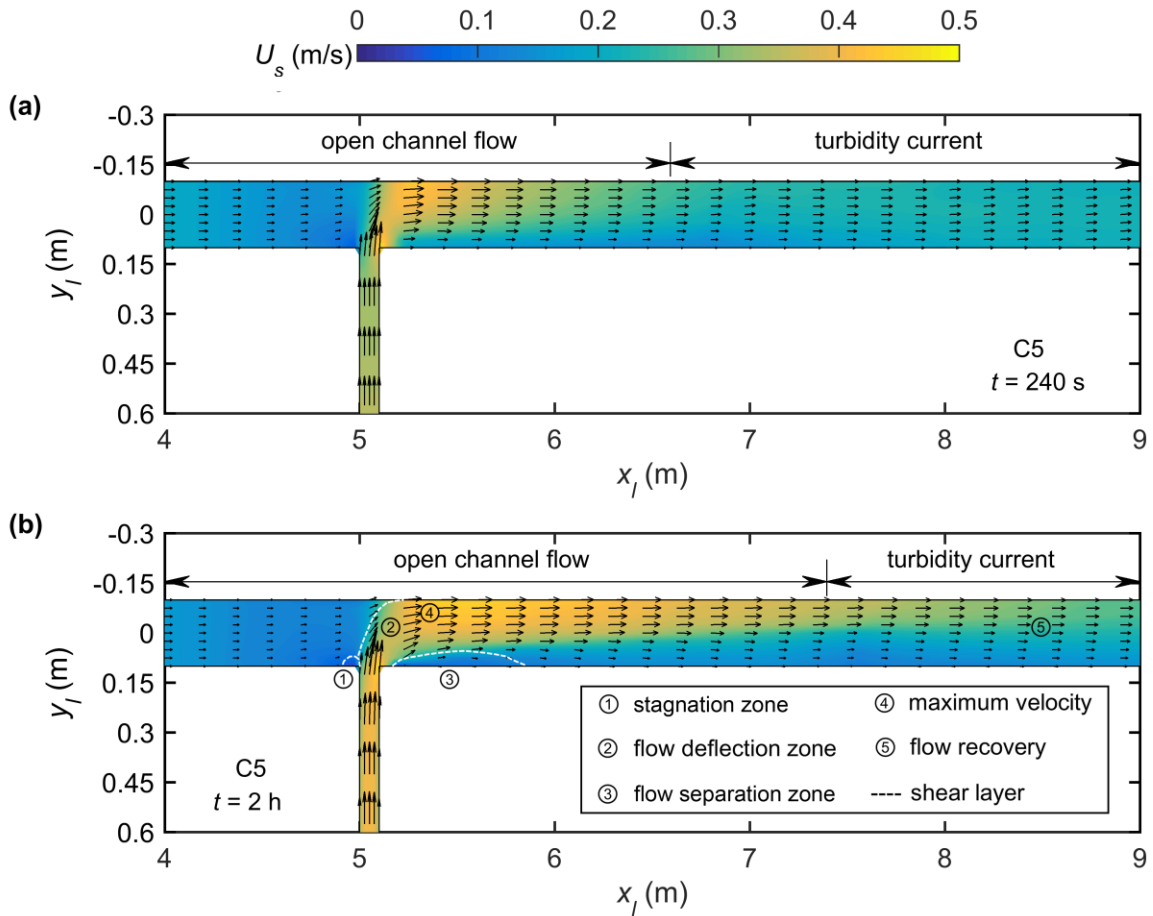


387
 388 **Fig. 8** Velocity field of sediment-laden flow layer for Case B3 when there is a turbidity
 389 current within the confluence, at times (a) $t = 240$ s, and (b) $t = 2$ h

390

391 As shown in Fig. 9, Case C5 features highly concentrated, sediment-laden flow arriving
392 from both the MC and the TR at a junction located upstream of the OSPP. By $t = 240\text{ s}$, the
393 sediment-laden flow in the TR has encountered the turbidity current in the MC. The turbidity
394 current plunges downstream of the junction, and the upper clear-water flow layer at the
395 confluence disappears (Figs. 3 and 5b). At this time, the layer-averaged velocity of the
396 sediment-laden flow at the confluence may be divided into the following zones: shear layers,
397 a stagnation zone near the upstream junction corner, a separation zone immediately after the
398 downstream junction corner, a deflection zone, an area of maximum velocity at the
399 confluence, and a flow recovery zone downstream of the junction. These resemble the flow
400 dynamic behavior at an open channel river confluence, proposed by Best [40]. The bed shear
401 stress magnitude is directly related to the velocity field of the sediment-laden flow layer, and
402 its value within the maximum velocity area is higher for Case C5 than for Case A1 without a
403 TR (Figs. 7b1 and 11b1). Later, by $t = 2\text{ h}$, the flow regions are more apparent with an
404 enlarged separation zone, driven by the long-term hydro-sediment-morphodynamic process
405 (Fig. 9b). Downstream of the junction, the bed shear stress is generally below 2.5 N/m^2 ,
406 except in the region of maximum velocity where the bed shear stress reaches about 5 N/m^2 .
407 In Case C5, the bed shear stress values are related to the sediment-laden flow velocity in the
408 vicinity of the confluence, and are higher than for Case A1 without a TR (Figs. 7b2 and
409 11b2).

410



412

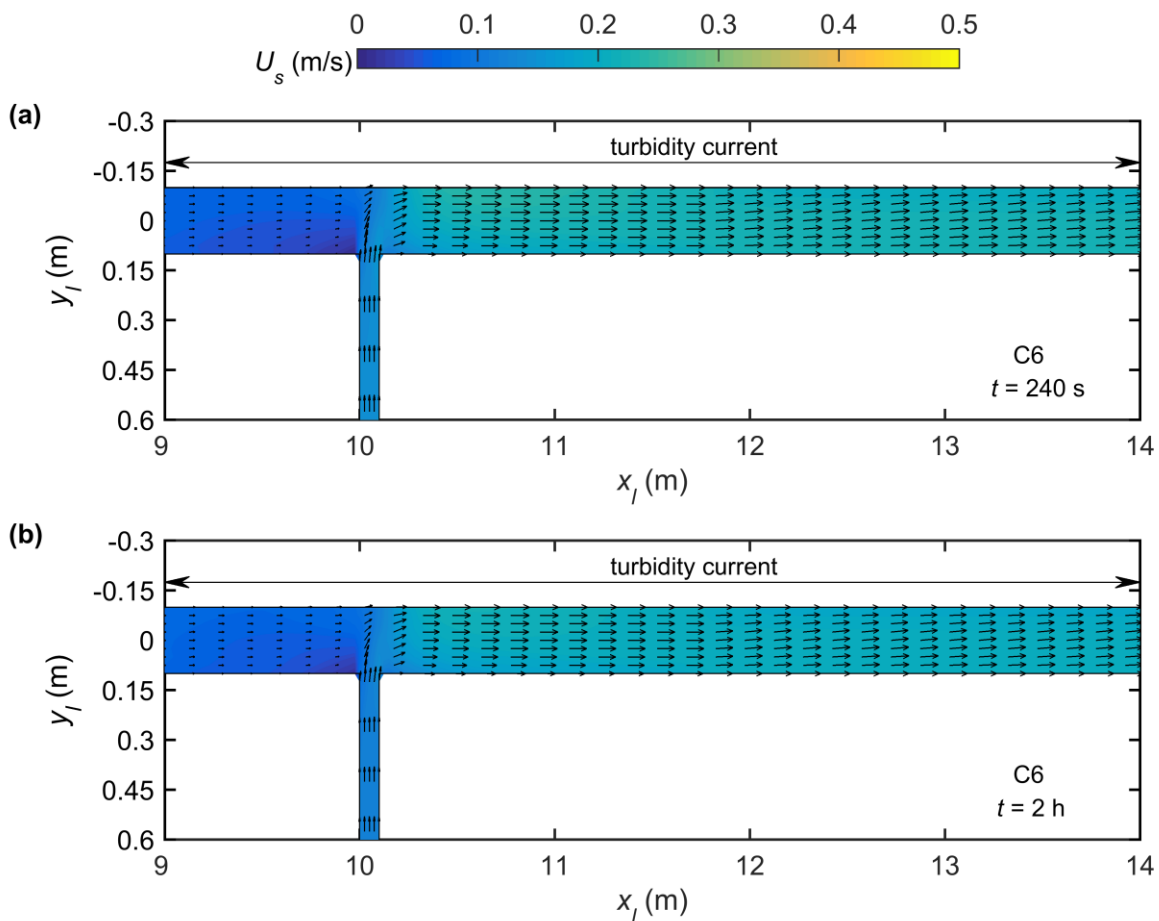
413 **Fig. 9** Velocity field of sediment-laden flow layer for Case C5 when there is open channel
 414 flow within the confluence, at times (a) $t = 240$ s, and (b) $t = 2$ h

415

416 Fig. 10 displays the lower-layer velocity field obtained for Case C6 which features
 417 upstream highly concentrated sediment-laden flow in both the MC and the TR. In this case,
 418 the junction is located downstream of the OSPP. By $t = 240$ s, the heavily sediment-laden
 419 flow from upstream in the TR has interacted with the MC turbidity current. The velocity field
 420 of the turbidity current reveals a stagnation zone near the upstream junction corner, a
 421 deflection zone, and a maximum velocity area at the confluence (Fig. 10a). Notably, flow
 422 separation cannot be discerned, although the minimum velocity observed downriver of the

423 downstream junction corner reaches zero. Compared with Case C5, the size of the separation
 424 zone is greatly affected by the junction location. The bed shear stress is minimized in the
 425 stagnation zone upstream of the junction, and reaches its highest level in the region of
 426 maximum velocity downstream of the junction (Fig. 11c1). Between $t = 240$ s and $t = 2$ h, the
 427 flow pattern and bed shear stress remain stable at the confluence (Fig. 10b). The bed shear
 428 stress downstream of the junction for Case C6 is approximately equal to 2.5 N/m^2 , higher
 429 than for Case A1 without a TR (Figs. 7b2 and 11c2).

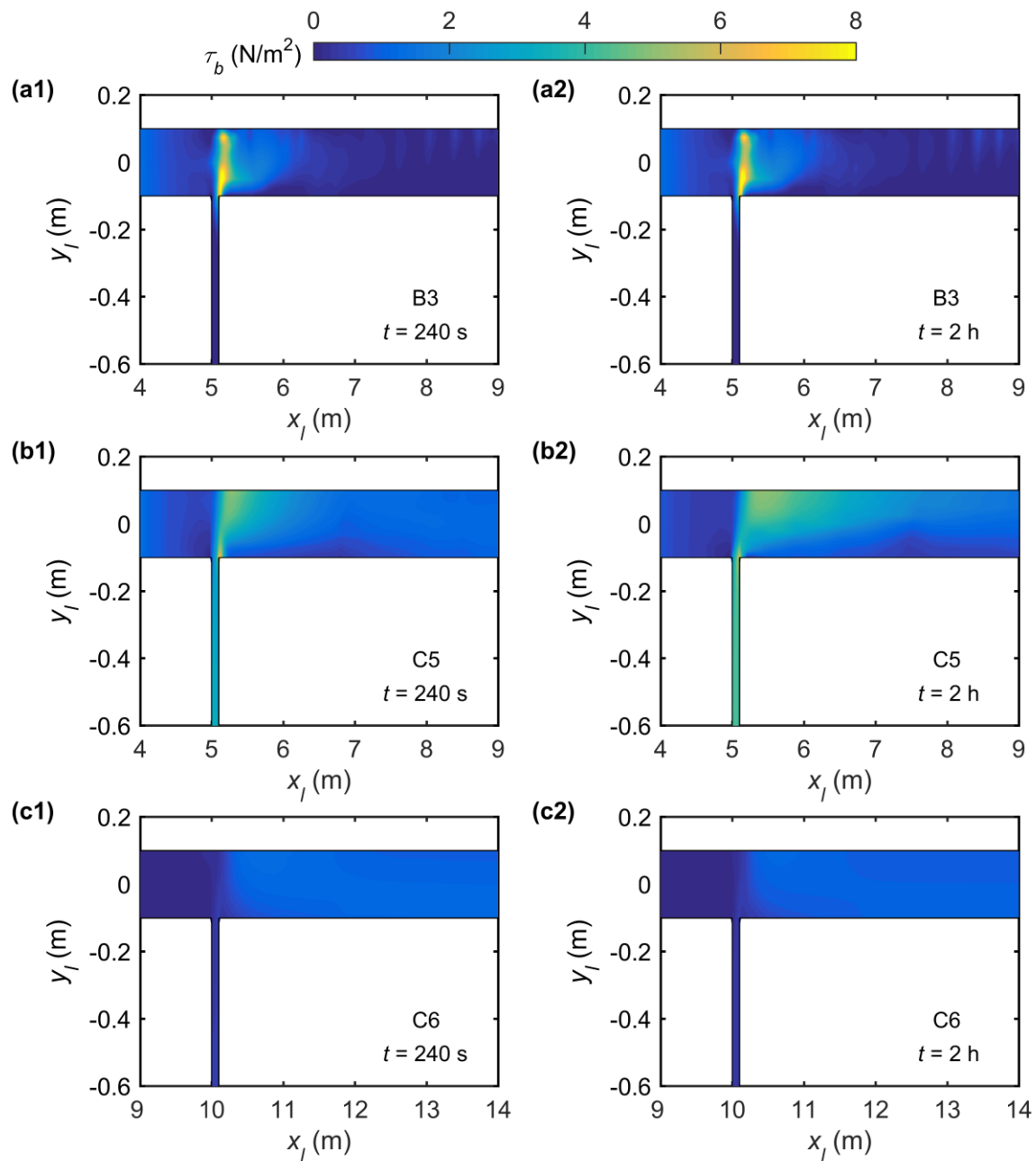
430



431

432 **Fig. 10** Velocity field of turbidity current within the confluence for Case C6, at times (a)

433 $t = 240$ s, and (b) $t = 2$ h



435

436 **Fig. 11** Planar distributions of bed shear stress τ_b magnitude at confluence at times $t = 240$ s437 and $t = 2$ h for **(a1-a2)** Case B3, **(b1-b2)** Case C5, and **(c1-c2)** Case C6

438

439 Significantly, two flow exchange patterns have distinct effects on the velocity field and

440 bed shear stress of the reservoir turbidity current. With the intrusion of reservoir turbidity

441 current from the MC to the TR, a lateral variation of turbidity current velocity occurs at the
442 confluence (Fig. 8), different from Case A1 that experiences changes solely in the
443 longitudinal velocity component (Fig. 7). With the heavily sediment-laden flow plunging
444 from the TR into the turbidity current in the MC, the flow dynamics near the confluence is
445 mainly affected by the junction location. For a junction located upstream of the OSPP, the
446 flow structure of the turbidity current at the confluence resembles the pattern described by
447 Best [40] (Fig 9). By contrast, features of the turbidity current velocity field effectively
448 disappear when the junction is located downstream of the OSPP, due to the increased layer
449 thickness of the turbidity current at the confluence (Figs. 6 and 10). Compared to the case
450 without a TR, the tributary inflow conditions cause the local bed shear stress to increase,
451 which can initiate sediment transport at the junction.

452

453 **3.5 Sediment transport**

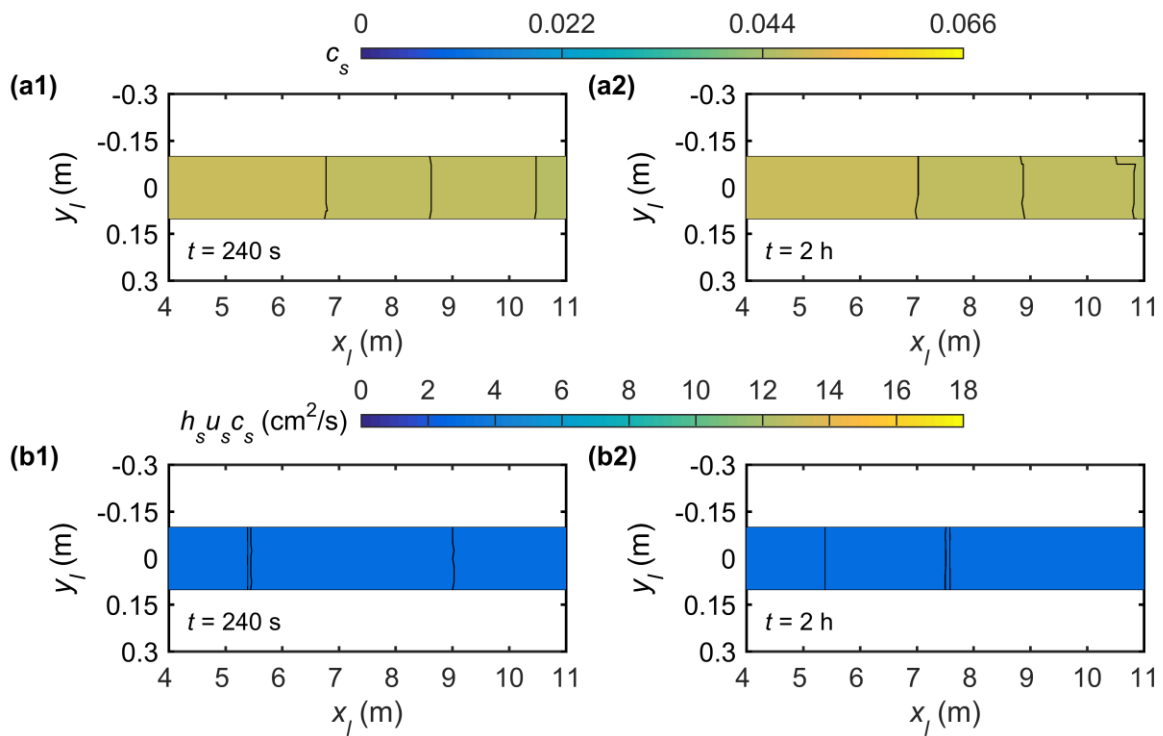
454 The effects of tributary inflow conditions on volumetric sediment concentration, and
455 longitudinal and transverse sediment transport rates per unit channel width are displayed in
456 Figs. 12-15 for Cases A1, B1-B4, and C1-C6.

457 In general, as the reservoir turbidity current propagates, the sediment concentration c_s
458 reduces longitudinally along the MC in the absence of TR (Fig. 12a1), while the longitudinal
459 sediment transport rate per unit width $h_s u_s c_s$ usually remains below $3.0 \text{ cm}^2/\text{s}$ (Fig. 12b1),
460 and there is no transverse sediment transport. On being vented through the BSFT, the
461 sediment concentration and sediment transport rate of the reservoir turbidity current exhibit

462 almost no change from $t = 240$ s to $t = 2$ h owing to the imposed steady upstream boundary
463 condition (Figs. 12a2 and 12b2). In cases where the TR is present, the situation is quite
464 different. In Cases B1 and B3, as the MC turbidity current intrudes into the junction,
465 sediment concentration in the TR decreases longitudinally, and the lowest sediment
466 concentration occurs at the intrusion front inside the TR (Figs. 13a and 13c). The longitudinal
467 sediment transport rate per unit width increases at the downstream junction corner (Figs. 14a
468 and 14c), while the transverse sediment transport rate per unit width at the central junction is
469 negative, being deflected by the inflow from the TR (Figs. 15a and 15c). Additionally, the
470 MC turbidity current further intrudes into the TR in Cases B2 and B4, for which the junction
471 is located downstream of the OSPP (Figs. 13b and 13d). In Cases C1-C6, as the
472 sediment-laden flow from the TR interacts with the reservoir turbidity current in the MC, the
473 longitudinal sediment transport rate per unit width downstream of the junction is increased
474 relative to Case A1 without a TR (Figs. 14e-14j).

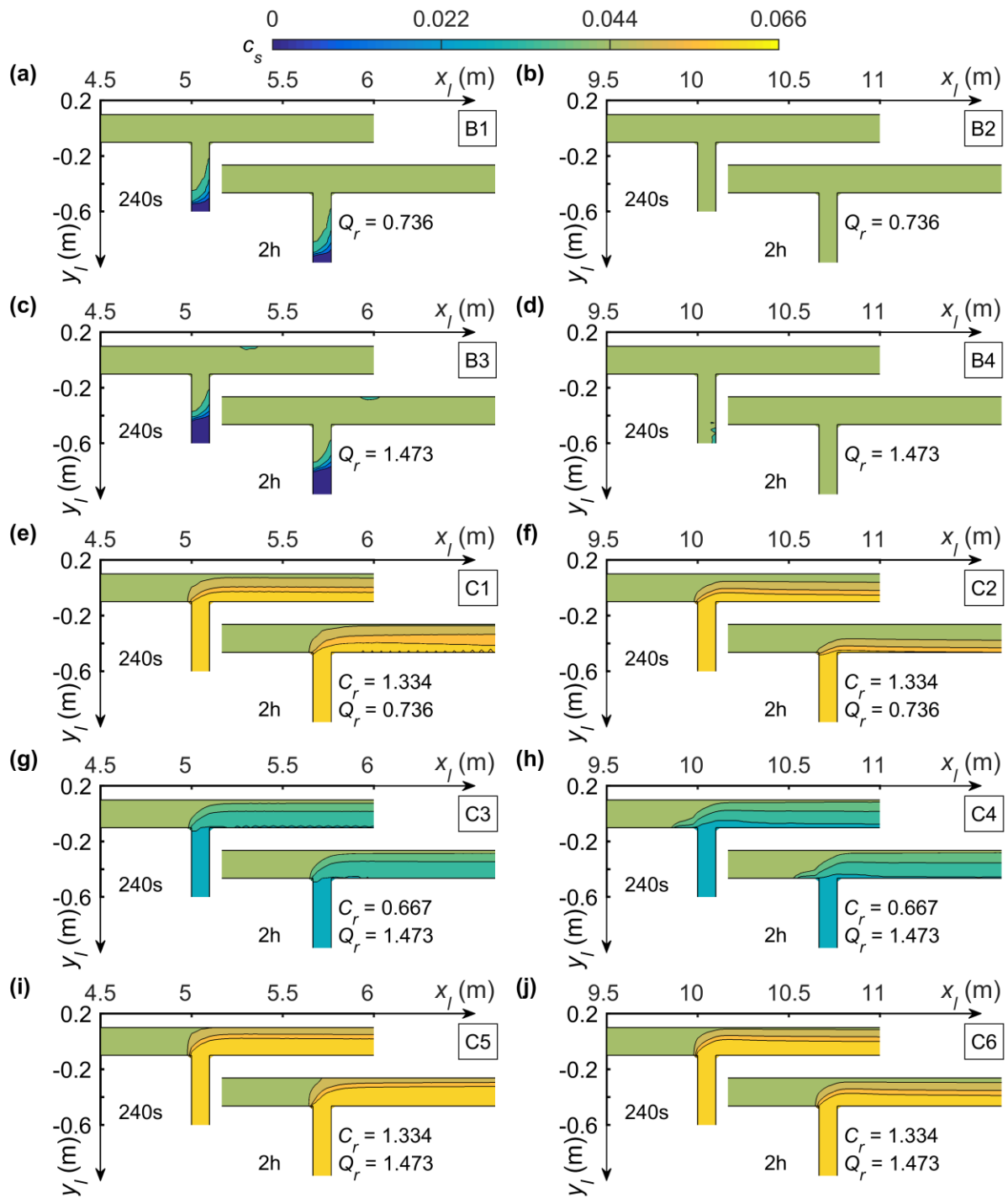
475 Our results for highly concentrated sediment transport at a confluence are noticeably
476 different from previous studies on river confluences carrying low sediment loads or clear
477 water [40, 46]. The discharge ratio, sediment concentration ratio, and junction location are
478 key factors that control sediment transport near a confluence. For a heavily sediment-laden
479 flow plunging from a TR into a turbidity current in the MC, the highest levels of sediment
480 concentration in the MC occur downstream of the flow deflection zone. As the discharge ratio
481 increases, the TR sediment concentration becomes more uniform (Figs. 13e and 13i, 13f and
482 13j). When the junction is located upstream of the OSPP, the longitudinal and transverse

483 sediment transport rates per unit width increase in the region of maximum velocity but
 484 decrease within the flow separation zone (Figs. 14i and 15i). When the junction is located
 485 downstream of the OSPP, the planar distribution of sediment transport rates is no longer
 486 evident because of the featureless flow dynamics at the confluence (Figs. 14j and 15j).
 487



488
 489 **Fig. 12 (a1-a2)** Volumetric sediment concentration c_s , **(b1-b2)** longitudinal sediment
 490 transport rate per unit width $h_s u_s c_s$ for Case A1 at times $t = 240$ s and $t = 2$ h

491

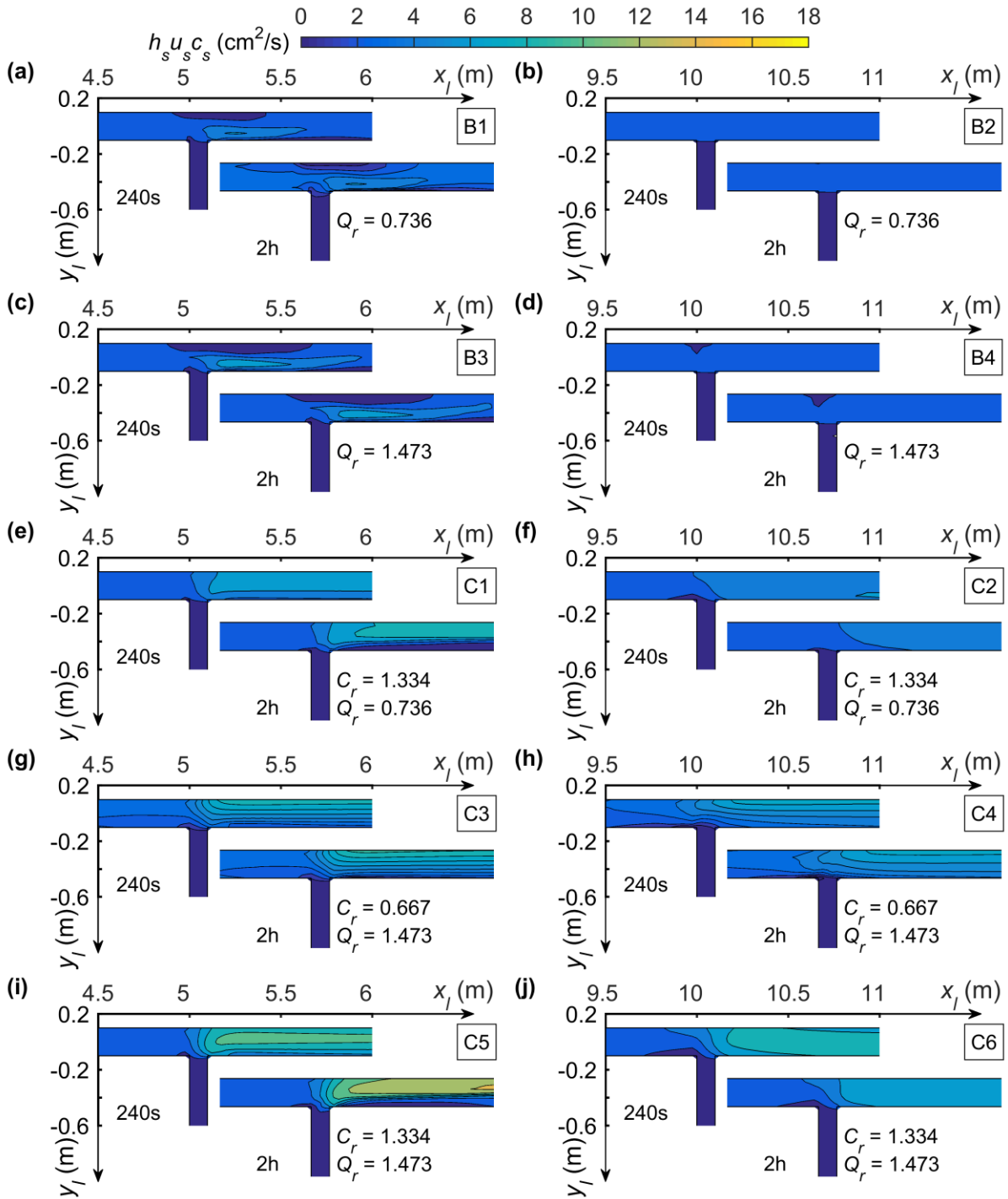


492

493 **Fig. 13** Volumetric sediment concentration c_s within the confluence at times $t = 240$ s and t

494 $= 2$ h for Cases B1-B4, and C1-C6 in (a) - (j)

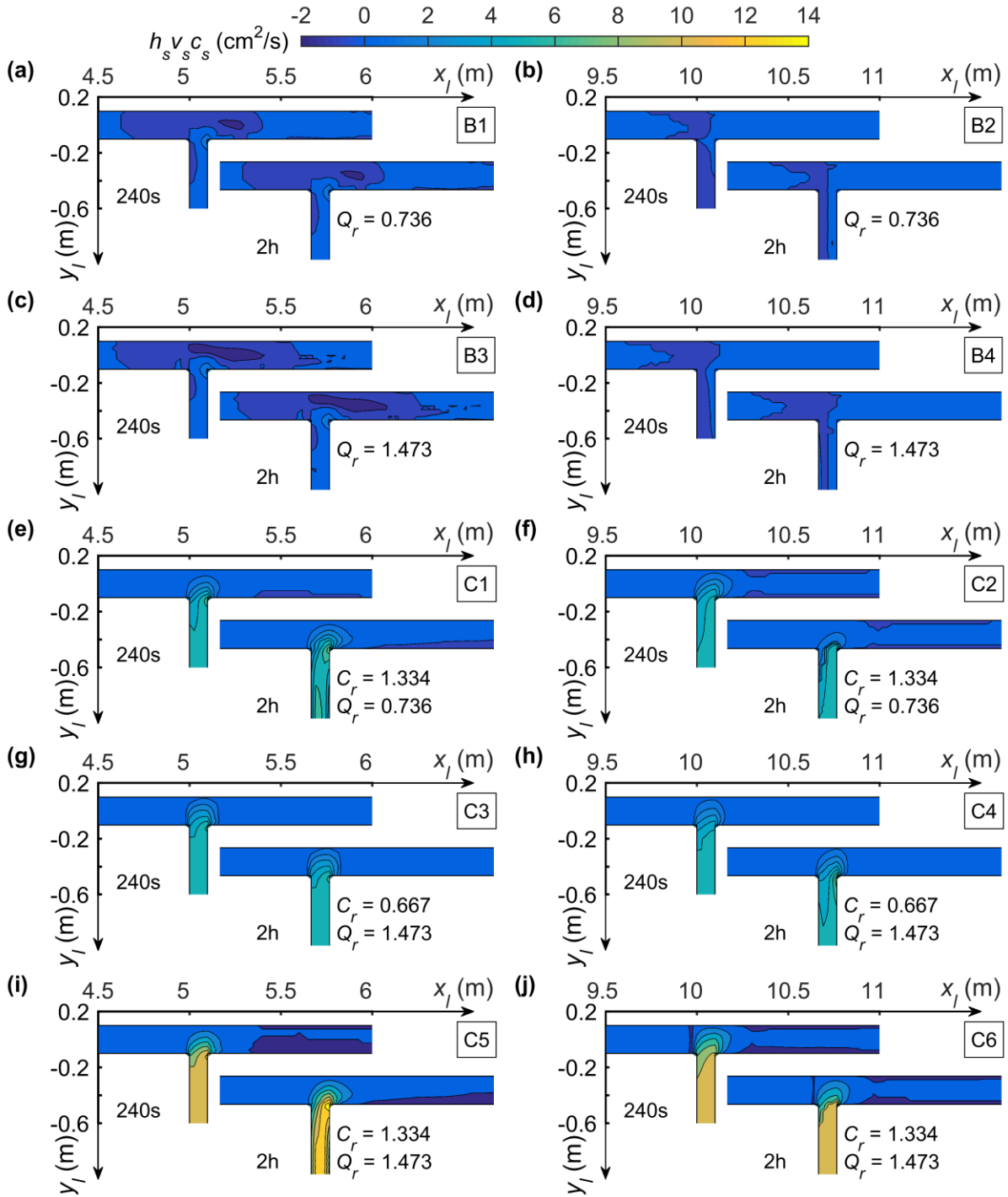
495



496

497 **Fig. 14** Longitudinal sediment transport rate per unit width $h_s u_s c_s$ within the confluence at
 498 times $t = 240$ s and $t = 2$ h for Cases B1-B4, and C1-C6 in (a) - (j)

499



500

501 **Fig. 15** Transverse sediment transport rate per unit width $h_s v_s c_s$ within the confluence at
 502 times $t = 240$ s and $t = 2$ h for Cases B1-B4, and C1-C6 in (a) - (j)

503

504 3.6 Bed deformation

505 Fig. 16 illustrates the spatial distribution of bed deformation depth, defined as

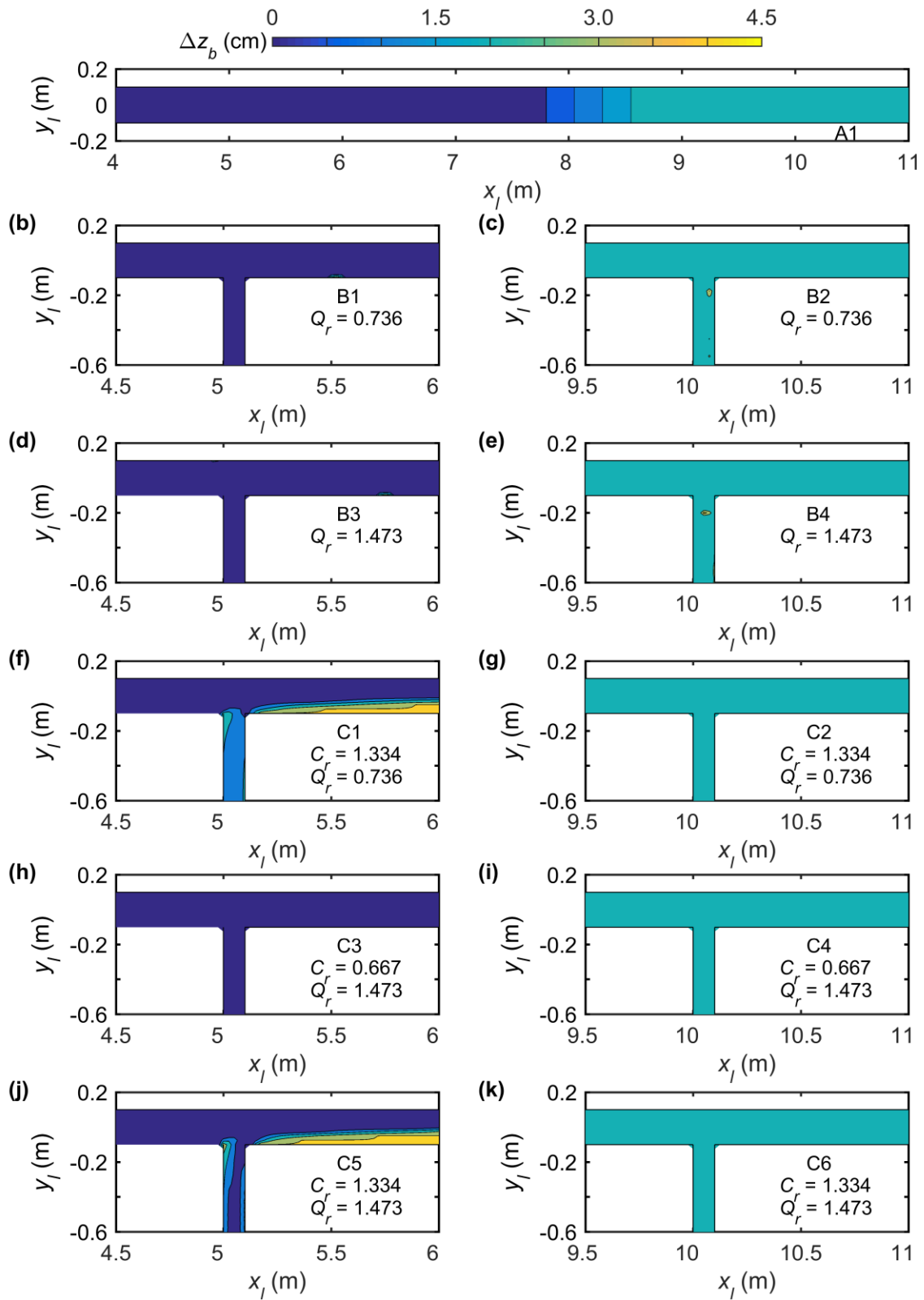
506 $\Delta z_b = z_b(x, y, t) - z_b(x, y, 0)$, at time $t = 2$ h, for Cases A1, B1-B4, and C1-C6. Comparison
507 between the Series B and Series C results in Fig. 16 helps reveal the impacts of junction
508 location, discharge ratio, and sediment concentration ratio on bed morphology at an idealized
509 river confluence.

510 Bed aggradation occurs upstream of the dam as the turbidity current propagates along
511 the MC (Fig. 16a). Tributary inflow conditions affect local bed deformation at the confluence.
512 Specifically, when the junction is located upstream of the OSPP and $C_r > 1$, as in Cases C1
513 and C5, the majority of sediment is conveyed downstream through the central junction, with
514 the remainder partly deposited in the flow stagnation and separation zones owing to the
515 reduced flow velocity (Figs. 16f and 16j). A thalweg is created at the TR extending a short
516 distance across the MC by sediment deposition in the flow stagnation zone and separation
517 zone. A separation zone bar extends downstream and towards the opposite side of the MC,
518 resembling bed deformation at a river confluence as described by Zhang et al. [32, 33]. The
519 flow separation zone is influenced by the discharge ratio [47], with a larger separation zone
520 bar occurring for Case C5 compared with that for Case C1 (Figs. 16f and 16j). The location
521 of the junction also has a profound effect on bed deformation. When the junction is located
522 upstream of the OSPP and $C_r < 1$, as in Cases B1, B3 and C3, bed deformation is hardly
523 discernible at the confluence (Figs. 16b, 16d and 16h). When the junction is located
524 downstream of the OSPP, as in Cases C2, C4 and C6, the width of the flow separation zone
525 decreases (Fig. 10), hindering formation of the separation zone bar (Figs. 16g, 16i and 16k).
526 Moreover, as the MC turbidity current intrudes into the junction in Cases B2 and B4, the

527 lower speed of the sediment-laden flow layer in the TR promotes sediment deposition and
528 bed aggradation inside the TR (Figs. 16c and 16e).

529 Tributary inflow has a significant effect on bed morphology at a river confluence. In
530 particular, the sediment concentration ratio and junction location provide the most important
531 controls on bed deformation. When both the MC and TR carry highly concentrated
532 sediment-laden flows and the junction is located upstream of the OSPP, the bed morphology
533 near the confluence develops a bar in the stagnation zone at the upstream junction corner, a
534 bar in the flow separation zone below the downstream junction corner, and a thalweg for
535 sediment transport through the central junction. These are in contrast with the scour hollow
536 and avalanche faces observed in previous research on river confluences with clear water or
537 low sediment loads [46, 48, 49]. Consequently, tributary inflow and sediment input
538 conditions dominate hydro-sediment-morphodynamic processes at a river confluence.

539



540

541 **Fig. 16** Spatial distribution of bed deformation depth Δz_b at $t = 2$ h for Cases A1, B1-B4,

542 and C1-C6 in (a) - (k)

543

544 3.7 Sediment flushing efficiency

545 We finally probe into how sediment flushing by a turbidity current is affected by the tributary
546 inflow. Here, sediment flushing efficiency is defined as the ratio of sediment volume (V_{so})
547 exiting the bottom outlet (driven by the turbidity current) to the total sediment volume (V_{si})
548 entering from the MC and TR, where V_{si} and V_{so} are calculated from

$$549 \quad V_{si}(t) = \iint (h_s u_s c_s)_{inlet} dy dt \quad (2)$$

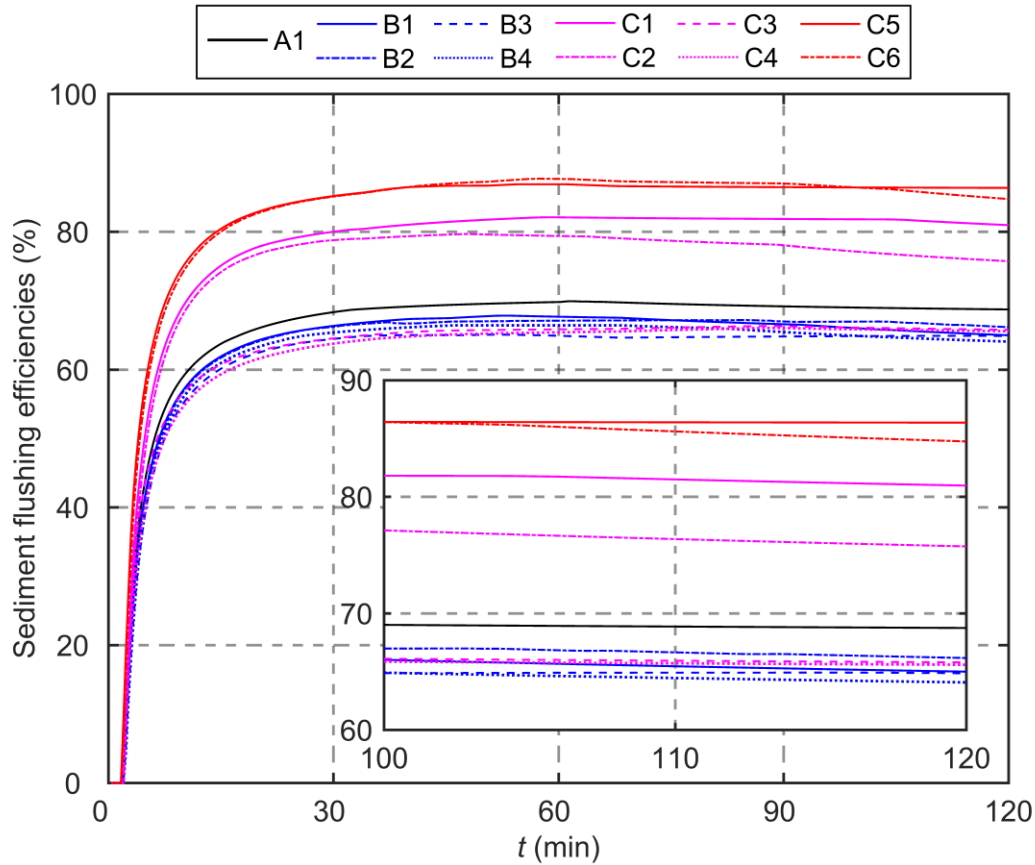
$$550 \quad V_{so}(t) = \iint (h_s u_s c_s)_{outlet} dy dt \quad (3)$$

551
552
553 Fig. 17 shows the evolution of sediment flushing efficiency for Cases A1, B1-B4, and
554 C1-C6 (Table 2). In general, sediment flushing initiates once the turbidity current front
555 reaches the bottom outlet. The flushing efficiency grows rapidly with time during the first 20
556 minutes or so, with the rate of increase slowing until a peak value is reached roughly at 1 hr,
557 after which the efficiency either decreases slightly (Cases C2 and C6) or saturates. At $t \sim 2$
558 min, as the turbidity current front arrives (Fig. 3), the bottom sluice gate is opened for
559 sediment flushing through the BSFT, allowing sediment to exit the MC. During the first 20
560 min, with increasing outflow discharge and sediment concentration, the sediment exit rate
561 increases, stimulating the flushing efficiency to increase rapidly. Subsequently, the outflow
562 discharge settles to a stable state as the turbidity current evolves upstream of the dam, whilst
563 the sediment output rate exhibits a similar trend. Thus, the flushing efficiency increases
564 slowly until reaching a peak at 1 hr. It should be noted that the sediment output decreases due
565 to severe long-term sediment deposition in cases involving a higher concentration ratio and a

566 junction located further downstream, such as Cases C2 and C6, (Figs. 16e and S4).

567 In Cases B1-B4, C3, and C4, the presence of clear-water or dilute sediment-laden flow
568 in the TR lowers the efficiency of sediment flushing compared with Case A1. In cases with a
569 TR, the MC turbidity current is diluted by the tributary inflow and the concurrent intrusion of
570 the MC turbidity current into the tributary. Both lead to a reduction in sediment concentration
571 of the MC turbidity current, and so cause the sediment flushing efficiency to fall. By contrast,
572 highly concentrated sediment-laden inflow from the TR reinforces the MC turbidity current,
573 thereby leading to higher sediment flushing efficiency as found in Cases C1, C2, C5, and C6.
574 Briefly, the effect of tributary inflow on sediment flushing efficiency by the turbidity current
575 is so significant that it should be taken into account in reservoir sedimentation management
576 and the maintenance of reservoir capacity.

577



578

579 **Fig. 17** Time histories of sediment flushing efficiency for different tributary inflow
 580 conditions

581

582 **3.8 Discussion**

583 3.8.1 Effects of tributary configuration

584 The numerical results presented in sections 3.1, 3.2 and 3.7 demonstrate that tributary inflows
 585 have an appreciable effect on the formation and propagation of MC turbidity current and
 586 sediment flushing efficiency. Here, the results are further extended for other parameter
 587 controls listed in Table 2 (i.e., tributary bed slope i_{br} , junction angle θ , and width ratio W_r),
 588 corresponding to Fig. 18 and Fig. S2 given in the Supporting Information online.

589 Compared to Case A1 without a TR, the MC turbidity current propagation is slower for
590 cases with clear-water inflow from upstream of the TR. If the junction is located downstream
591 of the OSPP, a larger width ratio W_r , a lower tributary bed slope i_{bt} , or a smaller junction
592 angle θ causes the turbidity current to propagate more slowly, demonstrated by the front
593 location in Cases B4, B8, B10, and B12 (Fig. 18b). However, these controls exert a minor
594 influence in cases where the junction is located upstream of the OSPP (Fig. 18a). This is
595 primarily because the width ratio W_r , tributary bed slope i_{bt} , and junction location together
596 control the intrusion distance of the turbidity current from MC to TR, leading to lower
597 sediment concentration and thus a smaller driving force for the MC turbidity current. Clear
598 water flow from the TR with discharge ratio $Q_r > 1$ and smaller junction angle $\theta = 45^\circ$
599 drives a longitudinal flow of the upper layer in the MC, which increases interface resistance
600 to the turbidity current and slows down the propagation of the turbidity current. The results
601 shown in Figs. 18a and 18b demonstrate that the foregoing controls have a slight influence on
602 the formation of MC turbidity current, corresponding to the location and depth at plunge
603 points along the central axis of the MC. However, this role cannot be neglected in cases
604 involving sediment-laden flow from upstream of the TR. Notably, for Cases B7-B12 with
605 clear water inflows from upstream of TR, the control parameters, W_r , i_{bt} , and θ , exert
606 minor influence on the efficiency of sediment flushing (Fig. S2).

607 Figs. 18c and 18d indicate that for sediment-laden inflow from the TR, even if the
608 tributary configuration is modified, it is still conducive to the propagation of the MC turbidity
609 current compared with Case A1 without the TR, and has a significant influence on plunge

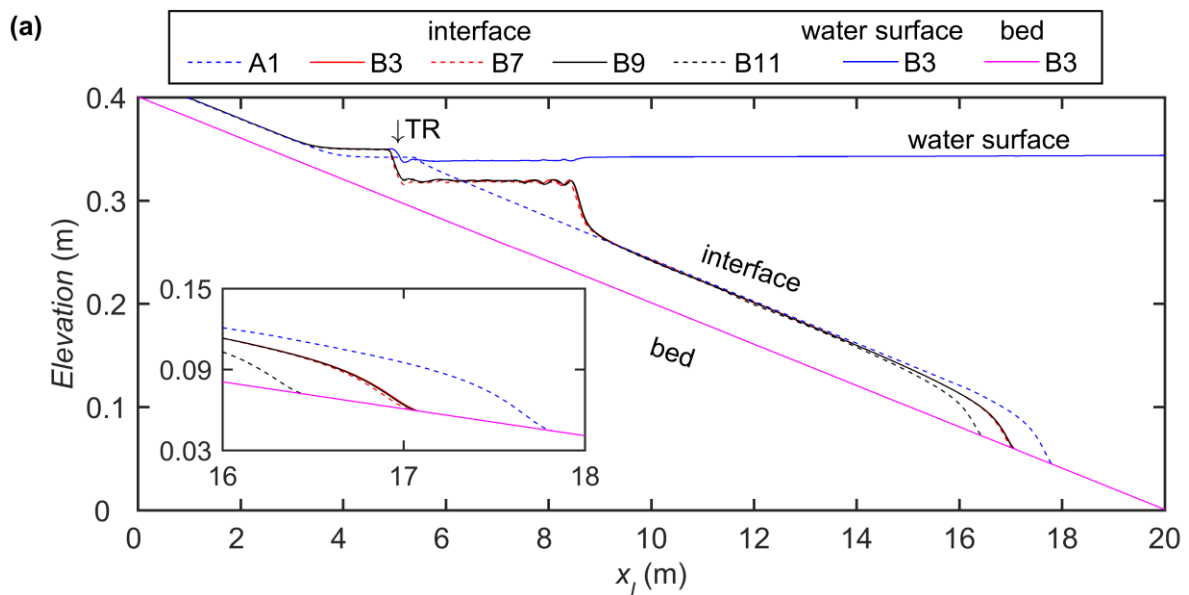
610 point location. Compared with Case C5, the distance between the plunge point and main
611 flume entrance increases discernibly with increasing width ratio W_r , but decreases with
612 increasing junction angle θ , corresponding to Cases C9 and C13. The influence of tributary
613 bed slope i_{bt} is minor. Notably, there is lateral variation in the plunge point position of Case
614 C13 with $\theta = 45^\circ$, which is quite distinct from that of Case C5 with $\theta = 90^\circ$ (see Fig. R3 in
615 the Support Information online). The turbidity current front located further downstream of the
616 MC has a higher tributary bed slope i_{bt} or a smaller junction angle θ , as in Cases C11 and
617 C13, C12 and C14. By contrast, a slower advance of turbidity current front is generally
618 obtained with larger width ratio W_r , corresponding to Cases C9 and C10. Physically, given
619 that the inflow discharge of TR is specified (Table 2), the velocity of sediment-laden flow
620 from upstream of the TR decreases in relation to a larger width ratio W_r . Therefore, due to
621 the later interaction time with the upstream sediment-laden flow entering from the TR, the
622 MC turbidity current propagates slowly (temporarily). For Cases C9-C14 involving heavily
623 sediment-laden inflows from TR, a larger width ratio W_r , or a higher tributary bed slope i_{bt} ,
624 or a smaller junction angle θ lowers sediment flushing efficiency compared with Cases C5
625 and C6 (Fig. S2). Sediment flushing efficiencies rise faster at first in cases with higher
626 tributary bed slope i_{bt} and smaller junction angle θ (i.e., Cases C12 and C14), and then
627 decrease slightly or saturate because of long-term sediment deposition in the MC. A tributary
628 configuration with a larger W_r apparently lowers the sediment flushing efficiency,
629 especially when the TR is located downstream of the OSPP.

630 Succinctly, although the tributary configuration modifies the interaction between MC

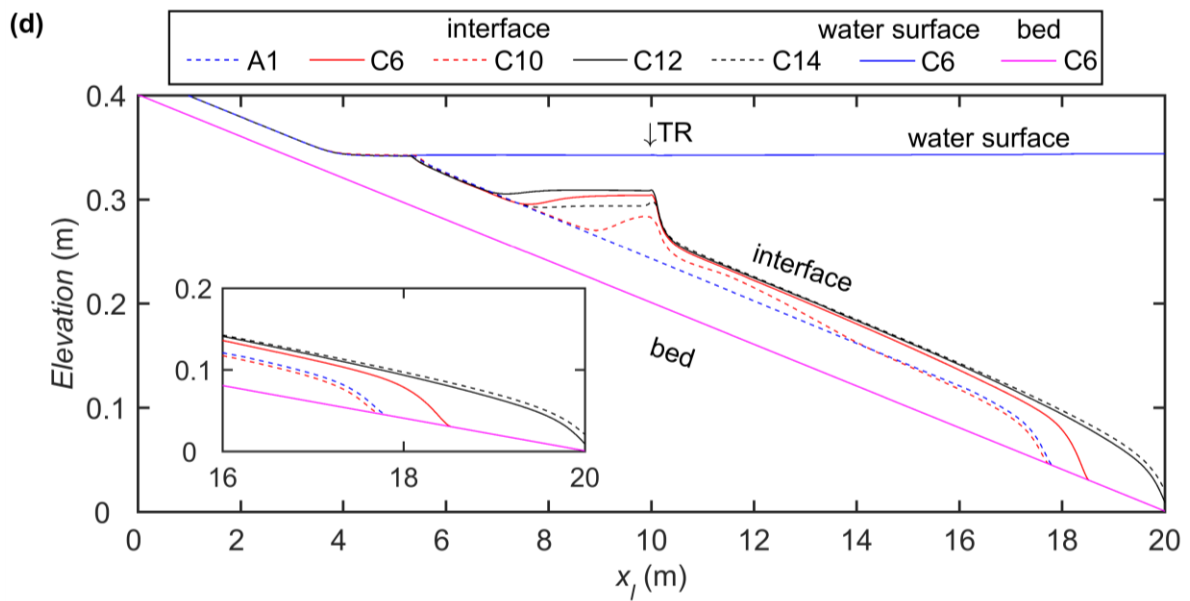
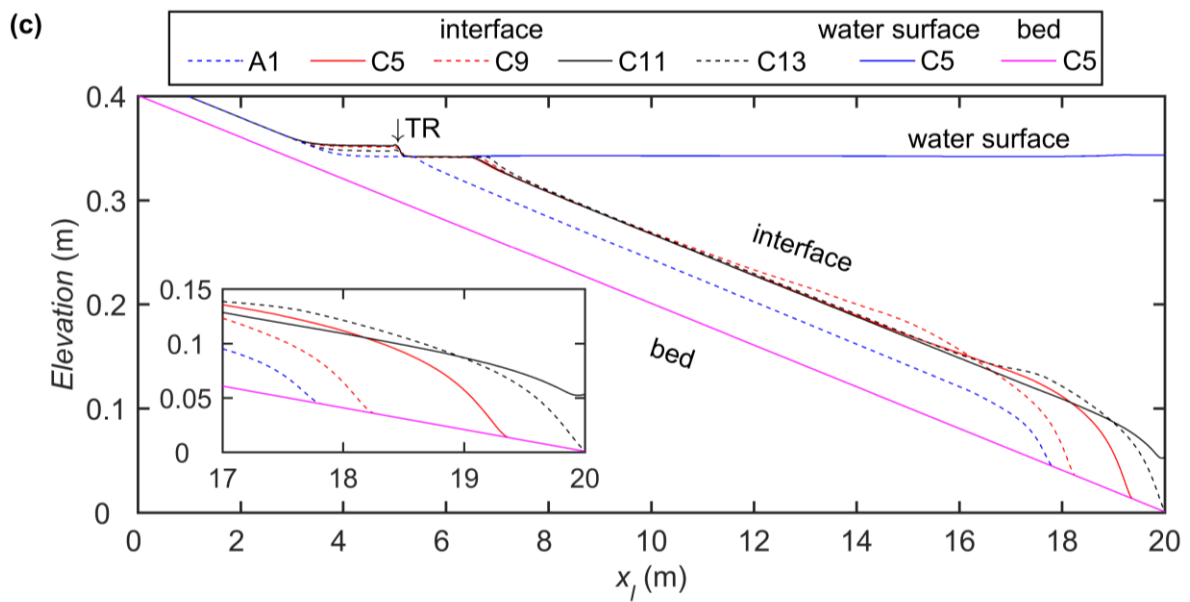
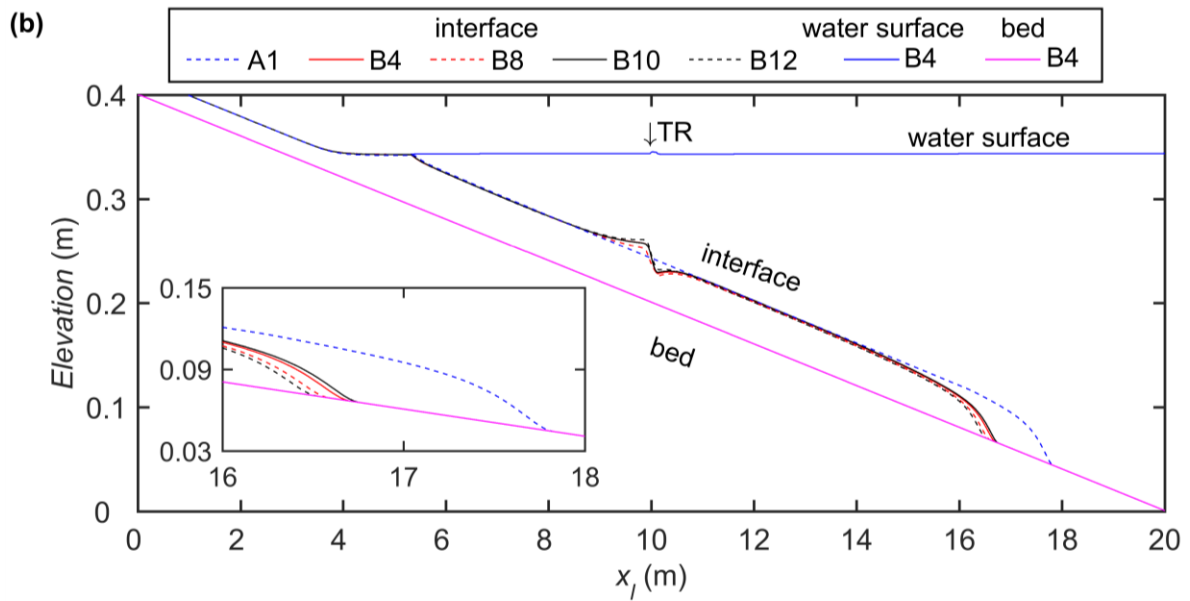
631 and TR, our findings concerning the effect of tributary inflow on reservoir turbidity current,
 632 as shown in Figs. 3-17, appear to hold. The presence of a tributary has significant
 633 implications for the advance of a turbidity current front and the efficiency of sediment
 634 flushing, which must be taken into account in the timely operation of bottom outlets under a
 635 dam so that sediment can be thoroughly flushed out of the reservoir.

636 The present computational study is limited to uniform sediment. It is intended to
 637 consider the effect of different sediment size distributions from the MC and TR on reservoir
 638 turbidity currents in a future study. Although this study has mainly focused on
 639 laboratory-scale cases, prototype-scale cases merit further investigation, such as the Guxian
 640 Reservoir, planned for the middle Yellow River, China.

641



642



644 **Fig. 18** Water surface, interface and bed profiles C14 along central axis of the MC at
645 $t = 100\text{s}$ for Cases: **(a)** A1, B3, B7, B9, and B11; **(b)** A1, B4, B8, B10, and B12; **(c)** A1, C5,
646 C9, C11, and C13; and **(d)** A1, C6, C10, and C12.

647

648 3.8.2 Dimensional analysis

649 To be included.

650

651 **4 Conclusion**

652 The following conclusions are drawn on the effect of a tributary on reservoir turbidity
653 currents, based on a parameter study using a 2D double layer-averaged computational model
654 [12].

655 Tributary effects on turbidity current formation and propagation in the MC mainly depend
656 on tributary discharge, sediment input, and junction location. Sediment concentration is the
657 primary control on sediment flushing efficiency. Tributary configuration (i.e., width ratio W_r ,
658 tributary bed slope i_{bt} , and junction angle θ) also appreciably modifies the propagation of
659 the turbidity current front and the sediment flushing efficiency. Clear water flow from the TR
660 may cause the stable plunge point to migrate upstream, reducing its thickness and sediment
661 concentration, leading to a slower front advance and a lower sediment flushing efficiency
662 than in a counterpart MC without tributary inflow. For cases with clear water flow from the
663 TR, it should be noted that a tributary configuration with larger W_r , lower i_{bt} , and smaller
664 θ leads to slower propagation of the turbidity current, and only minor influence on sediment

665 flushing efficiency. Sediment-laden inflow from the TR may cause the stable plunge points to
666 migrate downstream, increasing the discharge, thickness and sediment concentration of the
667 reservoir turbidity current, which is also conducive to propagation of the turbidity current.
668 Highly concentrated sediment-laden inflow from a TR leads to a considerably higher
669 sediment flushing efficiency by the turbidity current in the MC. Those effects are more
670 pronounced when the TR is located upstream of the OSPP. By contrast, when the junction is
671 located downstream of the OSPP, the TR has less effect on the formation and propagation of
672 the turbidity current. Furthermore, for cases with heavily sediment-laden flow from the TR,
673 smaller W_r , higher i_{bt} , and smaller θ all lead to faster propagation of the turbidity current.
674 A tributary configuration with larger W_r , higher i_{bt} , and smaller θ lowers sediment
675 flushing efficiency, especially when the TR is located downstream of the OSPP.

676 Tributary location and inflow conditions lead to complicated flow dynamics and bed
677 deformation at the confluence. The velocity field and spatial distribution of bed shear stress
678 of the reservoir turbidity current resemble their counterparts in a confluence flow with a low
679 sediment load or clear water. Yet, the sediment transport and bed deformation of a confluence
680 flow with high sediment concentrations are quite different from those at an ordinary
681 sediment-laden flow confluence. The discharge ratio and sediment concentration ratio are key
682 factors that control bed morphology close to the confluence. When the junction is located
683 upstream of the OSPP, the bed morphology of confluence flows with high sediment
684 concentrations is divided into a bar in the flow stagnation zone, a thalweg for sediment
685 transport through the central junction, and a bar in the flow separation zone, unlike the scour

686 hollow and avalanche faces that develop in river confluences with low sediment loads or
687 clear water.

688 The present findings indicate that it is important to account for tributary inflow with high
689 sediment load when analysing reservoir turbidity currents. The presence of tributary inflow
690 has significant implications for the formation and evolution of a reservoir turbidity current,
691 and hence the sediment management of reservoirs located along heavily sediment-laden
692 rivers. Nevertheless, further laboratory and field observations are needed to enhance our
693 understanding of bed morphology at a river confluence carrying high sediment loads,
694 especially when the sediment is non-uniform.

695

696 **Acknowledgments**

697 Information deleted for blind review.

698

699 **References**

- 700 1. Wang GQ, Xia JQ, Zhang HW (2002) Theory and practice of hyperconcentrated
701 sediment-laden flow in China. Advances in Hydraulics and Water Engineering - 13th
702 IAHR-APD Congress, Singapore.
- 703 2. Wang ZY, Qi P, Melching CS (2009) Fluvial hydraulics of hyperconcentrated floods in
704 Chinese rivers. Earth Surface Processes and Landforms 7(34): 981-993.
705 <https://doi.org/10.1002/esp.1789>
- 706 3. Wan ZH, Wang ZY (1994) Hyperconcentrated flow. IAHR monograph series. Balkema,
707 Rotterdam, The Netherlands

- 708 4. Clerici A, Perego S (2000) Simulation of the Parma River blockage by the Corniglio
709 landslide (Northern Italy). *Geomorphology* 33(1): 1-23.
710 [https://doi.org/10.1016/S0169-555X\(99\)00095-1](https://doi.org/10.1016/S0169-555X(99)00095-1)
- 711 5. Cao ZX, Pender G, Carling P (2006) Shallow water hydrodynamic models for
712 hyperconcentrated sediment-laden floods over erodible bed. *Advances in Water*
713 *Resources* 29(4): 546-557. <https://doi.org/10.1016/j.advwatres.2005.06.011>
- 714 6. Li W, Su Z, van Maren DS, Wang Z, de Vriend HJ (2017) Mechanisms of
715 hyperconcentrated flood propagation in a dynamic channel-floodplain system. *Advances*
716 *in Water Resources* 107: 470-489. <https://doi.org/10.1016/j.advwatres.2017.05.012>
- 717 7. Li W, van Maren DS, Wang ZB, de Vriend HJ, Wu B (2014) Peak discharge increase in
718 hyperconcentrated floods. *Advances in Water Resources* 67(4): 65-77.
719 <https://doi.org/10.1016/j.advwatres.2014.02.007>
- 720 8. Li W, Xie GH, Hu P, He ZG, Wang YJ (2019) Mechanisms of peak discharge increase in
721 the Yellow River floods and its influencing factors. *Journal of Hydraulic Engineering*
722 50(9): 1111-1122 (in Chinese). <https://doi.org/10.13243/j.cnki.slxh.20190103>
- 723 9. Best J (2019) Anthropogenic stresses on the world's big rivers. *Nature Geoscience* 12(1):
724 7-21. <https://doi.org/10.1038/s41561-018-0262-x>
- 725 10. Armanini A (2013) Granular flows driven by gravity. *Journal of Hydraulic Research*
726 51(2): 111-120. <https://doi.org/10.1080/00221686.2013.788080>
- 727 11. Cantero Chinchilla FN, Dey S, Castro Orgaz O, Ali SZ (2015) Hydrodynamic analysis of
728 fully developed turbidity currents over plane beds based on self - preserving velocity
729 and concentration distributions. *Journal of Geophysical Research: Earth Surface*
730 120(10): 2176-2199. <https://doi.org/10.1002/2015JF003685>
- 731 12. Cao ZX, Li J, Pender G, Liu QQ (2015) Whole-process modeling of reservoir turbidity
732 currents by a double layer-averaged model. *Journal of Hydraulic Engineering* 141(2):

- 733 04014069. [https://doi.org/10.1061/\(ASCE\)HY.1943-7900.0000951](https://doi.org/10.1061/(ASCE)HY.1943-7900.0000951)
- 734 13. Chamoun S, De Cesare G, Schleiss AJ (2016) Managing reservoir sedimentation by
735 venting turbidity currents: A review. *International Journal of Sediment Research* 31(3):
736 195-204. <https://doi.org/10.1016/j.ijsrc.2016.06.001>
- 737 14. Ford DE, Johnson MC (1983) An assessment of reservoir density currents and inflow
738 processes. Ford Thornton Norton and Associates LTD, Vicksburs Ms
- 739 15. Hu P, Cao ZX, Pender G, Tan GM (2012) Numerical modelling of turbidity currents in
740 the Xiaolangdi reservoir, Yellow River, China. *Journal of Hydrology* 464: 41-53.
741 <https://doi.org/10.1016/j.jhydrol.2012.06.032>
- 742 16. Wang Z, Xia J, Li T, Deng S, Zhang J (2016) An integrated model coupling open-channel
743 flow, turbidity current and flow exchanges between main river and tributaries in
744 Xiaolangdi Reservoir, China. *Journal of Hydrology* 543: 548-561.
745 <https://doi.org/10.1016/j.jhydrol.2016.10.023>
- 746 17. Xia CC (2019) Coupled mathematical modelling of shallow water flow and substance
747 transport in open channels (in Chinese). Wuhan University, Wuhan, China
- 748 18. Georgoulas AN, Angelidis PB, Panagiotidis TG, Kotsovinos NE (2010) 3D numerical
749 modelling of turbidity currents. *Environmental Fluid Mechanics* 10(6): 603-635.
750 <https://doi.org/10.1007/s10652-010-9182-z>
- 751 19. An S, Julien PY (2014) Three-dimensional modeling of turbid density currents in Imha
752 Reservoir, South Korea. *Journal of Hydraulic Engineering* 140(5): 05014004.
753 [https://doi.org/10.1061/\(ASCE\)HY.1943-7900.0000851](https://doi.org/10.1061/(ASCE)HY.1943-7900.0000851)
- 754 20. Lai YG, Huang J, Wu K (2015) Reservoir turbidity current modeling with a
755 two-dimensional layer-averaged model. *Journal of Hydraulic Engineering* 141(12):
756 04015029. [https://doi.org/10.1061/\(ASCE\)HY.1943-7900.0001041](https://doi.org/10.1061/(ASCE)HY.1943-7900.0001041)
- 757 21. Wang Z, Xia J, Zhang J, Li T (2018) Modeling turbidity currents in the Xiaolangdi

- 758 Reservoir with the effect of flow exchanges with tributaries. *Advanced Engineering*
759 *Sciences* 50(01): 85-93 (in Chinese). <https://doi.org/10.11660/slfdxb.20171205>
- 760 22. Dai A, Garcia M (2009) Analysis of plunging phenomena. *Journal of Hydraulic Research*
761 47(5): 638-642. <https://doi.org/10.3826/jhr.2009.3498>
- 762 23. Li Y, Zhang J, Ma H (2011) Analytical Froude number solution for reservoir density
763 inflows. *Journal of Hydraulic Research* 49(5): 693-696.
764 <https://doi.org/10.1080/00221686.2011.593905>
- 765 24. Lee HY, Yu WS (1997) Experimental study of reservoir turbidity current. *Journal of*
766 *Hydraulic Engineering* 123(6): 520-528.
767 [https://doi.org/10.1061/\(ASCE\)0733-9429\(1997\)123:6\(520\)](https://doi.org/10.1061/(ASCE)0733-9429(1997)123:6(520))
- 768 25. Li J, Cao ZX, Liu QQ (2019) Waves and sediment transport due to granular landslides
769 impacting reservoirs. *Water Resources Research* 55(1): 495-518.
770 <https://doi.org/10.1029/2018WR023191>
- 771 26. Li J, Cao ZX, Cui Y, Borthwick A (2020) Barrier lake formation due to landslide
772 impacting a river: A numerical study using a double layer-averaged two-phase flow
773 model. *Applied Mathematical Modelling* 80: 574-601.
774 <https://doi.org/10.1016/j.apm.2019.11.031>
- 775 27. Li J, Cao ZX, Cui Y, Fan X, Yang WJ, Huang W, Borthwick A (2021)
776 Hydro-sediment-morphodynamic processes of the Baige landslide-induced barrier Lake,
777 Jinsha River, China. *Journal of Hydrology* 596: 126134.
778 <https://doi.org/10.1016/j.jhydrol.2021.126134>
- 779 28. Xiong ZW, Xia JQ, Wang ZH, Li T, Zhang JH (2019) Whole-processes modeling of flow
780 movement and sediment transport during the period of water-sediment regulation in
781 Xiaolangdi Reservoir. *Scientia Sinica (Technologica)* 49(4): 419-432 (in Chinese).
782 <https://doi.org/10.1360/N092017-00295>

- 783 29. Zhang T, Feng MQ, Chen KL (2020) Hydrodynamic characteristics and channel
784 morphodynamics at a large asymmetrical confluence with a high sediment-load main
785 channel. *Geomorphology* 356: 107066. <https://doi.org/10.1016/j.geomorph.2020.107066>
- 786 30. Dou ST, Yu X, Zhang JH, Xie WM, Wang WZ, Du XK (2020) Process - based
787 modelling of tributary mouth sandbar evolution in a high sediment - load reservoir.
788 *River Research and Applications* 36(2): 199-210. <https://doi.org/10.1002/rra.3579>
- 789 31. Han QW (2003) Reservoir deposition (in Chinese). Science Press. Beijing, China
- 790 32. Zhang YF, Wang P, Wu BS, Hou SZ (2015) An experimental study of fluvial processes at
791 asymmetrical river confluences with hyperconcentrated tributary flows. *Geomorphology*
792 230: 26-36. <https://doi.org/10.1016/j.geomorph.2014.11.001>
- 793 33. Zhang YF, Wang P (2017) Deposition pattern and morphological process at
794 hyperconcentrated flow confluences in upper Yellow River. *Journal of Hydroelectric*
795 *Engineering* 36(12): 39-48 (in Chinese). <https://doi.org/10.11660/slfdx.20171205>
- 796 34. Bonnetaze RT, Hallworth MA, Huppert HE, Lister JR (1995) Axisymmetric
797 particle-driven gravity currents. *Journal of Fluid Mechanics* 294: 93-121.
798 <https://doi.org/10.1017/S0022112095002825>
- 799 35. Parker G, Fukushima Y, Pantin HM (1986) Self-accelerating turbidity currents. *Journal of*
800 *Fluid Mechanics* 171(3): 145-181.
801 <https://doi.org/https://doi.org/10.1017/S0022112086001404>
- 802 36. Zhang RJ, Xie JH (1993) Sedimentation research in China: Systematic selections (in
803 Chinese). China and Power Press. Beijing, China
- 804 37. Taylor EH (1944) Flow characteristics at rectangular open-channel junctions.
805 *Transactions of the American Society of Civil Engineers* 109(1): 893-902.
806 <https://doi.org/10.1061/TACEAT.0005772>
- 807 38. Webber NB, Greated CA (1966) An investigation of flow behaviour at the junction of

- 808 rectangular channels. Proceedings of the Institution of Civil Engineers 34(3): 321-334.
809 <https://doi.org/10.1680/iicep.1966.8925>
- 810 39. Best JL, Reid I (1984) Separation zone at open-channel junctions. Journal of Hydraulic
811 Engineering 110(11): 1588-1594.
812 [https://doi.org/10.1061/\(ASCE\)0733-9429\(1984\)110:11\(1588\)](https://doi.org/10.1061/(ASCE)0733-9429(1984)110:11(1588))
- 813 40. Best JL (1987) Flow dynamics at river channel confluences: implications for sediment
814 transport and bed morphology. Recent Developments in Fluvial Sedimentology 39(5):
815 27-35. <https://doi.org/10.2110/pec.87.39.0027>
- 816 41. Sukhodolov AN, Rhoads BL (2001) Field investigation of three-dimensional flow
817 structure at stream confluences: 2. Turbulence. Water Resources Research 37(9):
818 2411-2424. <https://doi.org/10.1029/2001WR000317>
- 819 42. Bradbrook KF, Lane SN, Richards KS, Biron PM, Roy AG (2001) Role of bed
820 discordance at asymmetrical river confluences. Journal of Hydraulic Engineering
821 127(5): 351-368. [https://doi.org/10.1061/\(ASCE\)0733-9429\(2001\)127:5\(351\)](https://doi.org/10.1061/(ASCE)0733-9429(2001)127:5(351))
- 822 43. Ribeiro ML, Blanckaert K, Roy AG, Schleiss AJ (2012) Flow and sediment dynamics in
823 channel confluences. Journal of Geophysical Research 117(F1): F01035.
824 <https://doi.org/10.1029/2011JF002171>
- 825 44. Lyubimova T, Lepikhin A, Konovalov V, Parshakova Y, Tiunov A (2014) Formation of
826 the density currents in the zone of confluence of two rivers. Journal of Hydrology
827 508(1): 328-342. <https://doi.org/10.1016/j.jhydrol.2013.10.041>
- 828 45. Ismail H, Viparelli E, Imran J (2016) Confluence of density currents over an erodible bed.
829 Journal of Geophysical Research: Earth Surface 121(7): 1251-1272.
830 <https://doi.org/10.1002/2015JF003768>
- 831 46. Best JL (1988) Sediment transport and bed morphology at river channel confluences.
832 Sedimentology 35(3): 481-498. <https://doi.org/10.1111/j.1365-3091.1988.tb00999.x>

- 833 47. Shaheed R, Yan X, Mohammadian A (2021) Review and comparison of numerical
834 simulations of secondary flow in river confluences. *Water* 13(14): 1917.
835 <https://doi.org/10.3390/w13141917>
- 836 48. Herrero H, Díaz Lozada JM, García CM, Szupiany R, Best J, Pagot M (2017) The
837 influence of tributary flow density differences on the hydrodynamic behavior of a
838 confluent meander bend and implications for flow mixing. *Geomorphology* 304: 99-112.
839 <https://doi.org/10.1016/j.geomorph.2017.12.025>
- 840 49. Sambrook Smith GH, Nicholas AP, Best JL, Bull JM, Dixon SJ, Goodbred S, Sarker MH,
841 Vardy ME (2019) The sedimentology of river confluences. *Sedimentology* 66(2):
842 391-407. <https://doi.org/10.1111/sed.12504>
- 843